Parallel transmission for ultrahigh-field imaging

Francesco Padormo[a], Arian Beqiri[a], Joseph V. Hajnal[a,b] and Shaihan J. Malik[a]*

The development of MRI systems operating at or above 7 T has provided researchers with a new window into the human body, yielding improved imaging speed, resolution and signal-to-noise ratio. In order to fully realise the potential of ultrahigh-field MRI, a range of technical hurdles must be overcome. The non-uniformity of the transmit field is one of such issues, as it leads to non-uniform images with spatially varying contrast. Parallel transmission (i.e. the use of multiple independent transmission channels) provides previously unavailable degrees of freedom that allow full spatial and temporal control of the radiofrequency (RF) fields. This review discusses the many ways in which these degrees of freedom can be used, ranging from making more uniform transmit fields to the design of subject-tailored RF pulses for both uniform excitation and spatial selection, and also the control of the specific absorption rate. © 2015 The Authors. *NMR in Biomedicine* published by John Wiley & Sons Ltd.

Keywords: ultrahigh-field MRI; parallel transmission; RF shimming; SAR; B_1 mapping

INTRODUCTION

Recent years have seen increased popularity of human MRI systems operating at ultrahigh magnetic field strength ($B_0 \geq 7$ T). However, operating at ultrahigh field (UHF) creates an additional set of technical challenges which need to be solved before it can be widely adopted. These problems originate from the interaction of the patient with the electromagnetic fields to which they are exposed during the course of an MRI examination. Although these interactions are present during examinations at lower field strengths, they are more severe for UHF MRI and therefore result in more significant image artefacts. The higher Larmor frequency (and consequently shorter electromagnetic radiation wavelength) results in wave interference effects becoming more pronounced (1–4). This manifests itself as inhomogeneity in both the transmit and receive radiofrequency (RF) magnetic fields, B_1^+ and B_1^-. Although more spatially variable receive fields result in better parallel imaging performance (5,6), non-uniformities in the transmit field lead to spatially varying flip angles. This can result in spatially varying contrast and, in the worst cases, regions in which no excitation can be achieved at all. Furthermore, the precise pattern of inhomogeneity is subject dependent (7). A multitude of solutions have been proposed to address the problems associated with B_1^+ inhomogeneities, such as the use of adiabatic RF pulses (8,9), dielectric pads (10–12) and dedicated coil designs (13,14). However, the most flexible approach is the use of multiple transmission channels, known as parallel transmission (PTx), which is the subject of this review.

The concept of multiple transmitters was proposed by Hoult (15) and Ibrahim et al. (16) in 2000. The paper by Hoult investigated the fundamental limits of B_1^+ homogeneity achievable by the use of multiple coils to 'shim' the B_1^+ field in an analogous manner to B_0 shimming. The first consideration of the use of multiple channels in a realistic loaded coil was performed by Ibrahim in a finite-difference time-domain numerical simulation

study, in which improved B_1^+ field homogeneity was obtained with a birdcage coil by driving each rung with a different phase.

Interest in PTx increased greatly after the demonstration of RF pulse acceleration by Katscher et al. (17) and Zhu (18). It was these papers that realised that PTx could provide full spatial and temporal control of the RF field, an idea which the

---

* Correspondence to: S. J. Malik, King's College London, Division of Imaging Sciences and Biomedical Engineering, The Rayne Institute, 3rd Floor Lambeth Wing, St Thomas' Hospital, London, SE1 7EH, UK.
E-mail: shaihan.malik@kcl.ac.uk

a F. Padormo, A. Beqiri, J. V. Hajnal, S. J. Malik
   Department of Biomedical Engineering, Division of Imaging Sciences and Biomedical Engineering, King's College London, King's Health Partners, St Thomas' Hospital, London, UK

b J. V. Hajnal
   Centre for the Developing Brain, Division of Imaging Sciences and Biomedical Engineering, King's College London, King's Health Partners, St Thomas' Hospital, London, UK

Abbreviations used: *2D/3D, two/three dimensional; CoV, coefficient of variation; DSC, direct signal control; EPG, extended phase graph; EPI, echo planar imaging; FOV, field of view; FSE, fast spin echo; HW, hardware; LC, linear combination; LEx, local excitation; LLS, linear least squares; LTA, large tip angle; MaxMin, maximise the minimum; MLS, magnitude least squares; MP-RAGE, magnetisation-prepared rapid gradient echo; PatLoc, parallel imaging technique using local gradients; PNS, peripheral nerve stimulation; PSS, pseudo-steady state; PTx, parallel transmission; RF, radiofrequency; ROI, region of interest; SAR, specific absorption rate; SLR, Shinnar Le-Roux; SMS, simultaneous multi-slice; SNR, signal-to-noise ratio; SPINS, spiral nonselective; SR-EPG, spatially resolved extended phase graph; STA, small tip angle; TEM, transverse electromagnetic; TIAMO, time-interleaved acquisition of modes; UHF, ultrahigh field; VERSE, variable rate selective excitation; VOP, virtual observation point.*

---

research community has latched on to with great enthusiasm. PTx has now transitioned from a purely research topic into clinical practice. Two channel transmitters are installed as standard in the latest clinical 3T systems from the major vendors, and many new 7T scanners are now equipped with multiple transmit channels.

This review explains the fundamentals and latest developments of PTx in its many different forms. This is achieved by classification of the methods based on the different time frames at which differences between channels are exploited. We begin with 'static PTx', where the transmit settings are optimised once at the beginning of the experiment and then remain fixed for the rest of the scan. This is followed by 'dynamic PTx', where differences between channels are exploited at the shortest time frames allowed by the system spectrometer. The intermediate area of 'multi-pulse PTx' is then examined, followed by a discussion of further topics relevant to PTx.

FUNDAMENTAL CONCEPTS

PTx systems differ from standard scanners by their RF system architecture. The key component of a PTx system is the transmit coil array, which must consist of several elements designed to produce spatially distinct RF field patterns. Each is driven by its own RF front end, consisting of multiple components. Although many different specific RF front ends have been proposed in the literature (19–23), for full PTx, all channels must be independently driven with full control over amplitude and phase modulation with microsecond temporal resolution. Each channel-specific waveform requires a separate RF amplifier in order to deliver the required power to each coil array element.

When driven with an RF pulse, the ith transmit element produces RF magnetic and electric fields, denoted by $\boldsymbol{B}_{1,i}(\mathbf{r}, t)$ and $\boldsymbol{E}_i(\mathbf{r}, t)$, respectively. The NMR-active component of $\boldsymbol{B}_{1,i}(\mathbf{r}, t)$ is referred to as $B_{1,i}^+(\mathbf{r},t) = \frac{1}{2}[B_{1,i}^x(\mathbf{r},t) + jB_{1,i}^y(\mathbf{r},t)]$ (24,25), where the x and y directions are perpendicular to the static magnetic field and $j = \sqrt{-1}$.

The different forms of PTx can be understood by further examining how they impact on the spatiotemporal nature of the transmit field. According to the principle of superposition, the net B_1^+ produced inside the subject is the sum of the fields produced by each element, as given by Equation [1a], where N_T is the number of transmit elements. However, the spatial and temporal components of $B_{1,i}^+$ can be separated, as shown in Equation [1b]. Here, $S_i(\mathbf{r})$ is the spatial 'footprint' of a transmit element, often referred to as the transmit sensitivity, and $p_i(t)$ is the RF pulse played through the ith transmitter. This equation describes 'dynamic PTx', in which each coil element transmits its own channel-specific waveform. A further simplification is shown in Equation [1c], where the same RF pulse waveform, $p(t)$, is transmitted on each channel, scaled by a channel-specific complex weight, w_i. This equation describes 'static PTx'. The final form of PTx described by this paper is 'multi-pulse PTx', in which the channel-specific weights or waveforms can change throughout an MR sequence.

$$B_1^+(\mathbf{r}, t) = \sum_{i=1}^{N_T} B_{1,i}^+(\mathbf{r}, t) \qquad [1a]$$

$$B_1^+(\mathbf{r}, t) = \sum_{i=1}^{N_T} p_i(t) S_i(\mathbf{r}) \qquad [1b]$$

$$B_1^+(\mathbf{r}, t) = p(t)\sum_{i=1}^{N_T} w_i S_i(\mathbf{r}) \qquad [1c]$$

All PTx methods rely on some degree of prior knowledge of $S_i(\mathbf{r})$ of each channel. This is achieved by 'B_1^+ mapping', which is discussed later in this article. Full knowledge of $S_i(\mathbf{r})$ constitutes the measurement of its amplitude and its phase relative to every other element at every location in space. It should be noted that there are many ways to define the units of $S(\mathbf{r})$, w_i and $p(t)$ in a dimensionally consistent manner; the specific selection by a user will probably depend on the specifics of the PTx system being used. Unless stated otherwise, the figures in this paper consider sensitivity maps as dimensionless.

The electric fields generated by each element also play an important role in PTx experiments, as it is the electric field which is responsible for heating, with the specific absorption rate (SAR) used as a surrogate metric. Regulatory agencies place limits on temperature increases and on local and whole-body SAR (26). SAR is a particular concern with PTx MRI because the total electric field (which is the result of a linear superposition of fields from each transmit channel) becomes spatially and temporally variable, potentially making 'hot spots' in unexpected locations. Many of the methods described in this review attempt to explicitly control SAR, often by using electric field information taken from numerical models. SAR is discussed in more detail later in the review.

Once the desired level of transmit and electric field information has been collected or inferred, it can be used to design the inputs to each of the transmit channels. Much PTx research has focused on the design of channel inputs with two separate goals in mind: (i) to overcome the effects of B_1^+ inhomogeneity; and (ii) to achieve local excitation (LEx).

B_1^+ inhomogeneity compensation can be achieved by all three forms of PTx. In this review, we adopt the following terminology for clarity: B_1^+ shimming refers to the use of static PTx to produce a spatially uniform overall B_1^+ field; flip angle shimming refers to the use of dynamic PTx to produce a spatially uniform flip angle; and signal shimming refers to the use of multi-pulse PTx to ensure that each tissue type produces a spatially uniform signal in any measured image.

However, it is important to note that, whatever the desired goal (i.e. compensation for B_1^+ inhomogeneity, achievement of LEx or something more elaborate), there are generic algorithms with which the channel inputs can be determined. These different methods are described in the following sections.

STATIC PTX

The most basic form of parallel transmission is static PTx, whose goal is to create the optimal conditions in a region of interest (ROI) by adjusting the complex weights (w_i) with which the individual channels are driven, defined by Equation [1c].

What constitutes 'optimal' depends on the specific application, but the majority of static PTx demonstrations have focused on B_1^+ shimming. Initial methods specified the objective of uniform B_1^+ across the slice or volume being imaged (15,16,27–29). Alternative pragmatic approaches were simultaneously being explored experimentally. The first physical implementation of B_1^+ shimming demonstrated that the B_1^+ field could be optimised in specific

voxels using a two-port birdcage coil at 3 T (30). It was also shown that manual B_1^+ shimming using operator intervention yielded more uniform images at UHF (31–33). However, it was soon realised that demanding uniformity across the entire imaged slice can be overly restrictive. One way of improving performance is to demand uniformity only over a smaller ROI – this particularly makes sense when imaging structures that are smaller than the field of view (FOV) and was originally explored in the context of 7T prostate imaging (34,35). As phase typically varies slowly in space, simply aligning the average phase of each channel within the ROI often leads to a good solution (35), as all channels are constructively interfering within the target region. This method has the advantage of not requiring the measurement of full B_1^+ information. The second realisation to aid B_1^+ shimming was that the appearance of an image often critically depends on the magnitude of the transmit field, and that its spatial phase distribution is often unimportant. Hence, B_1^+ shimming algorithms could relax their constraints, enabling solutions with a more homogeneous magnitude and inhomogeneous phase to be found (29,36–38).

Other static PTx methods have been designed with specific applications in mind. For example, adiabatic pulses are only effective when the B_1^+ amplitude is above the adiabatic threshold. Therefore, methods have been designed to maximise the minimum (MaxMin) B_1^+ without constraining uniformity, so that the adiabatic condition is met across the object (39,40). Another static PTx method obtains the weights which produce the largest overall B_1^+ amplitude per unit power deposited in the patient (41).

The use of static PTx for LEx has also been explored (42–45). The utilised cost functions typically attempt to maximise the ratio of the B_1^+ field in a desired ROI to the B_1^+ field outside the ROI. These methods have not yet been widely adopted, as they require a large number of transmit channels to achieve the required localisation in order to perform reduced FOV imaging; instead, LEx usually requires the design of full RF waveforms via dynamic PTx, as discussed later.

The majority of static PTx methods determine optimum weights by solving a numerical optimisation problem, typically by iteratively minimising a cost function. Many different cost functions have been proposed, with most consisting of error terms to constrain the spatial B_1^+ distribution (Φ_{target}), limit SAR (Φ_{SAR}) and ensure the results are within hardware limits (Φ_{HW}).

Static PTx optimisation problems are posed in one of three ways. The first is the regularised optimisation approach, in which the different penalised terms are added together, weighted by the regularisation factors λ and μ, as given in Equation [2a]. The cost function is typically solved for multiple values of λ and μ; these form a family of solutions with differing trade-offs between cost terms, often visualised using 'L-curves' showing the size of the component error terms. The solution that offers the best compromise is selected. The second related approach is the constrained optimisation framework (Equation [2b]). This enables the optimum of the B_1^+ constraint term to be found for given SAR and hardware limits.

$$\text{minimise } \Phi_{\text{tot}} = \Phi_{\text{target}} + \lambda\Phi_{\text{SAR}} + \mu\Phi_{\text{HW}} \quad [2a]$$

$$\text{minimise } \Phi_{\text{target}} \quad [2b]$$
$$\text{subject to } \Phi_{\text{SAR}} < SAR_{\text{max}}$$
$$\Phi_{\text{HW}} < HW_{\text{max}}$$

A selection of the different Φ_{target} used in different static PTx methods is given in Table 1. The sensitivity matrix **S** is constructed from the B_1^+ field information of all N_T channels in a user-defined ROI of N_{ROI} voxels. The information in the ROI from the ith transmitter is reshaped into an $N_{\text{ROI}} \times 1$ column vector $\mathbf{s}_i$, all of which are horizontally concatenated, so that $\mathbf{S} = [\mathbf{s}_1, \mathbf{s}_2 \ldots, \mathbf{s}_{N_T}]$. The $N_T \times 1$ vector **w** contains the complex weights to each channel, and $N_{\text{ROI}} \times 1$ vector **b** contains the desired B_1^+ field distribution.

Details of the SAR constraints can be found in the SAR section later in this review. For the sake of brevity, the additional hardware constraints are not described further, except to note that the most common additional constraint is for peak instantaneous power, which is related to max{|**w**|}; detailed explanations are given in refs. (46–48).

The third approach to obtain weights is to calculate them algebraically. These approaches do not require the use of optimisation algorithms as they can be found by simple arithmetic (35) or by performing matrix eigendecompositions (41).

Illustrative examples of several static PTx strategies are shown in Fig. 1. Figure 1A considers prostate imaging at 7 T using an eight-channel dipole array (49). Transmitting with the default weights of unit amplitude and zero phase (relative to an arbitrary reference) on each channel produces an overall B_1^+ field which is high at the periphery and low in the ROI. Phase shimming results in a larger B_1^+ field in the ROI, but the greatest field focusing is achieved using the maximum efficiency method. It should be noted that all solutions are scaled to have the same power (where power = $\mathbf{w}^H\mathbf{w}$). Examining the weights themselves, the phase shimming algorithm is constrained to produce weights with the same amplitude for all channels. The maximum efficiency approach can reweight channels appropriately to produce a more efficient result. However, it should be noted that phase shimming does not require full B_1^+ field information, which can be difficult to acquire at 7 T.

Figure 1B demonstrates two static PTx methods for a sagittal brain slice using simulated data from a 12-channel transverse electromagnetic (TEM) head coil. Again, it should be noted that all solutions are scaled to have the same power. The default weights produce a field with a very large dynamic range. The MaxMin algorithm produces a B_1^+ field which maximises the lowest realised field in the slice, providing improved performance for adiabatic pulses. However, the overall non-uniformity remains, making these weights inappropriate for imaging using non-adiabatic pulses. Using the coefficient of variation (CoV)

Table 1. Example cost function terms Φ_{target} used to constrain B_1^+ in static parallel transmission (PTx) optimisation problems

Field constraints	Cost function term	References
Linear least squares (LLS)	$\|\mathbf{Sw} - \mathbf{b}\|_2^2$	(15,16,27–29)
Magnitude least squares (MLS)	$\||\mathbf{Sw}| - \mathbf{b}\|_2^2$	(36–38)
Coefficient of variation (CoV)	$\dfrac{\text{std}(|\mathbf{Sw}|)}{\text{mean}(|\mathbf{Sw}|)}$	(29,34)
Maximise the minimum (MaxMin)	$\max(\min(|\mathbf{Sw}|))$	(39,40)
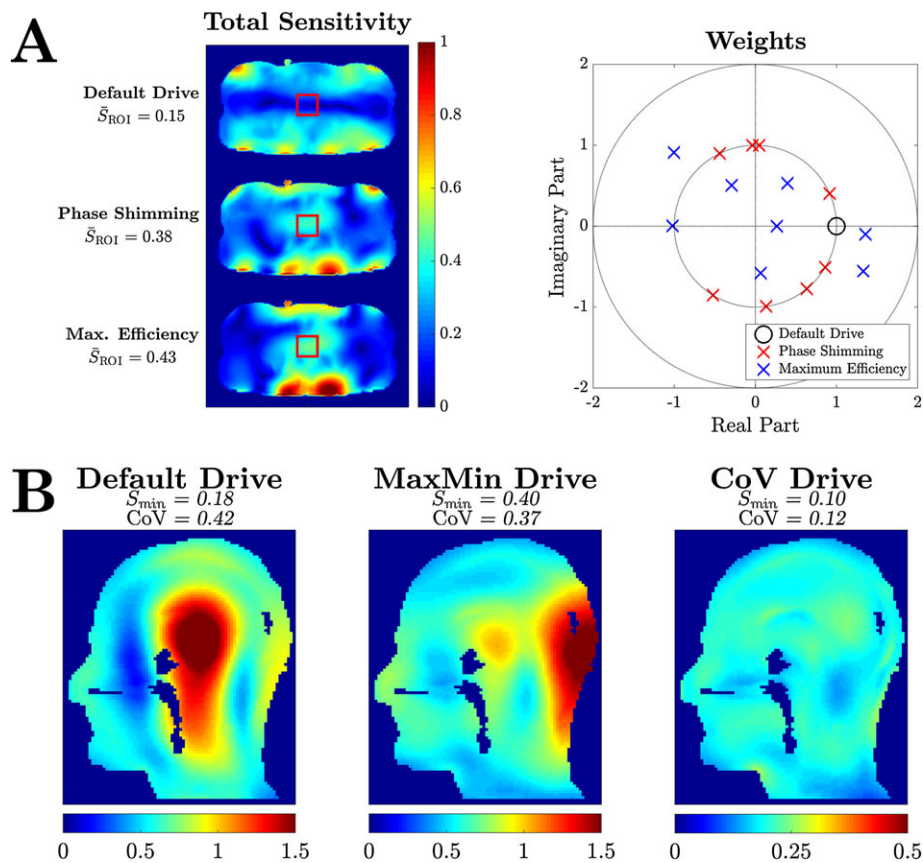
Figure 1. Illustrative example of B_1^+ shimming. (A) Net transmit sensitivities produced by a 7T, eight-channel dipole array when transmitting with default drives (top left), phase shimming (centre left) and maximum efficiency (bottom left). The prostate is indicated by the red box. The average sensitivities in the regions of interest (ROIs) are given by $\overline{S}_{ROI}$. The weights obtained for each method are given on the right. (B) Net transmit sensitivities produced by a 7T, 12-channel transverse electromagnetic (TEM) array with default drives (left), static parallel transmission (PTx) weights which maximise the minimum B_1^+ (centre), and applying weights which minimise the coefficient of variation (right). The minimum sensitivity in each slice is given by S_{min}. (Data courtesy of Dr Alessandro Sbrizzi, Dr Alexander Raaijmakers and Dr Hans Hoogduin, UMC Utrecht, the Netherlands).

metric produces a much more uniform B_1^+ appropriate for imaging, but with a much lower mean amplitude as the solution is very inefficient in terms of power.

The efficacy of static PTx has been widely demonstrated, particularly for two-channel birdcage systems at 3 T, where B_1^+ shimming has resulted in improved and more reliable imaging in many different clinical imaging scenarios (50–57), including imaging near metal implants (58). Furthermore, it has been shown that increasing the number of channels from two to eight improves the performance of 3T *in vivo* body imaging (59), and further studies have shown further improvements with up to 32 channels (60,61). B_1^+ shimming has also been applied *in vivo* at UHF. Much work has focussed on the brain, with multiple imaging demonstrations at both 7 T (62–66) and 9.4 T (19,33,67–69), in addition to spectroscopy (70–73). 7T body imaging has increased in popularity, with B_1^+ shimming being applied to cardiac (74–79), musculoskeletal (41,80–83), prostate (35,49,84–86), liver (87) and kidney (88–90) imaging.

DYNAMIC PTX

Static PTx is fundamentally limited to using the principle of superposition to achieve the goals of the pulse designer. Although it provides considerable control over B_1^+, for many imaging scenarios, the ability to achieve the desired B_1^+ across large FOVs

at UHF is limited by the degrees of freedom provided by constructively and destructively interfering a finite number of transmit sensitivities (29,60,61). However, additional flexibility can be gained by recognizing that what is actually desired is a 'flip angle' distribution, which depends on the overall rotation of the magnetisation and not just the instantaneous B_1^+. Dynamic PTx modulates the B_1^+ field distribution over the shortest timescales, with the aim of directly controlling the rotation of magnetization, and hence the overall flip angle, at multiple spatial locations simultaneously. In this framework, the capabilities of PTx can extend far beyond that which is achievable with static PTx alone.

The behaviour of magnetisation is described by the Bloch equation. However, its non-linear behaviour in the transverse magnetisation when rotations are large is difficult to incorporate into pulse design algorithms, and so the small tip angle (STA) approximation is often made (91). This simplifies the pulse design problem and introduces the concept of 'transmit k-space' ($\mathbf{k}(t)$, as defined by Equation [3]) to account for the effect of magnetic field gradients applied during the RF pulse.

$$\mathbf{k}(t) = -\gamma \int_t^T \boldsymbol{G}(t')\, \mathrm{d}t' \qquad [3]$$

Here T is the duration of the pulse and $\boldsymbol{G}(t)$ is the applied field gradient on all three axes. The key difference between transmit k-space and the more often used quantity for image encoding

is the limits on the integral; in the transmit case, the integration runs from 'now into the future', whereas, for image encoding, the limits run from 'the end of the excitation until now'. This can be understood by considering that, as the RF pulse is played out, new transverse magnetisation is being created, which is then subject to all future applied gradients. The STA approximation is used for the majority of current PTx pulse design algorithms (17,18,92), with the spatial domain approach (92) widely adopted as it is sufficiently flexible to incorporate B_0 inhomogeneity, arbitrary transmit k-space trajectories and spatial error weightings. As with static PTx, the pulses are obtained by minimising a cost function, posed in the same manner as Equation [2a] or [2b]. An example using regularised optimisation with a linear least-squares (LLS) error term and total RF power constraint is given by Equation [4]. Here, $\mathbf{p}$ is a vector containing the RF pulses of all transmit channels, $\mathbf{m}$ is the desired transverse magnetisation vector and $\mathbf{A}$ is the system matrix, which contains all information about the excitation k-space trajectory and the transmit field patterns. The terms in Equation [4] are closely related to those in cost functions used for static PTx. The vector $\mathbf{p}$ can be considered to contain time-variable weights for the N_P intervals in the RF pulse; Equation [4] reduces to the static PTx optimisation for the case when $N_P = 1$.

$$\text{minimise } \Phi_{\text{tot}} = \|\mathbf{Ap} - \mathbf{m}\|_2^2 + \lambda\|\mathbf{p}\|_2^2 \qquad [4]$$

This linear problem can be solved using a number of methods, such as conjugate gradients (93), and calculations can be accelerated by taking advantage of non-uniform fast Fourier transforms (94). As with static PTx, many alternative cost functions have been proposed. If a spatially varying magnetisation phase is tolerable, the magnitude least-squares (MLS) method can again be applied (37,38). Optimisations that

account for SAR (18,46,47,95–98), hardware (46,48) or even thermal effects (99) can also be formulated in this framework, and these can be solved using regularised or constrained optimisations (46,47).

Given the above possibilities in formulating the cost function, the remaining issue becomes the choice of k-space trajectory. There are broadly two classes of trajectory – those used for flip angle shimming and those used for LEx. These are discussed in the next two sections.

Dynamic PTx for flip angle shimming

PTx pulse design has been employed in cases in which B_1^+ shimming cannot achieve a sufficiently uniform flip angle across an ROI. A variety of different k-space trajectories have been proposed, falling broadly into the two categories shown in Fig. 2; those that require slice or slab selection (top row), and those which can be non-selective (bottom row). The selective trajectories are formed of individual 'spokes' which each provide slice selectivity – a single spoke is equivalent to a single slice-selective pulse. Additional in-plane spatial modulation is achieved by employing multiple spokes that are offset in k-space; typically, these offsets correspond to low spatial frequency modulations, reflecting the spatial length scale of the B_1^+ inhomogeneity (38,100–103). The same RF waveform is used along each spoke in order to retain selectivity; consequently, the only quantities to be optimised are complex weightings of each subpulse for each channel, making these optimisation problems inherently two-dimensional (2D) in nature. An example spoke RF pulse optimisation is illustrated in Fig. 3, which compares MLS B_1^+ shimming with a five-spoke RF pulse, solved using both LLS and MLS approaches discussed earlier and additionally employing the multi-shift algorithm (104). The L-curve in Fig. 3 shows the trade-off between flip angle accuracy (horizontal axis) and power (vertical axis) when solving the optimisation problems with
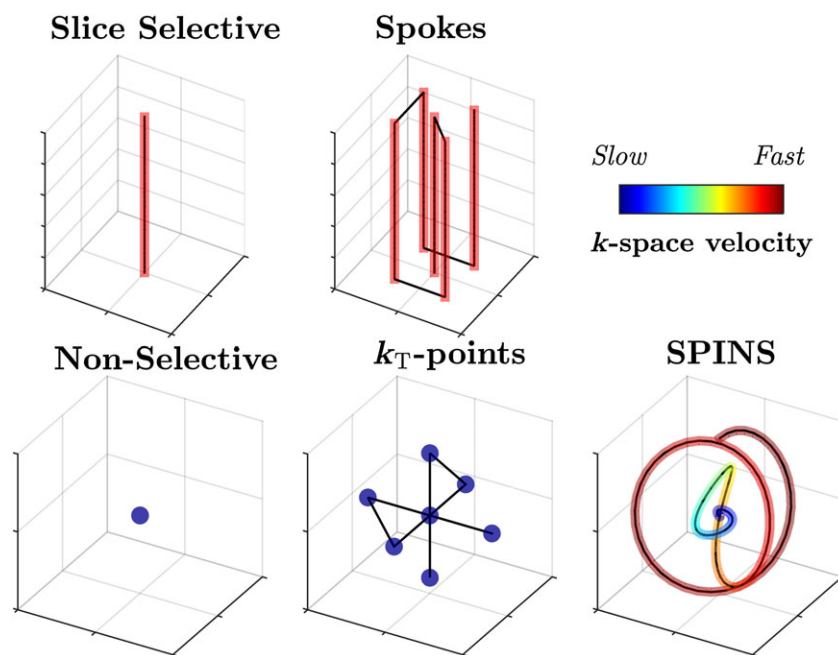
Figure 2. k-space trajectories for flip angle shimming. Black lines indicate the path through k-space, and shaded regions indicate where radiofrequency (RF) transmission occurs, with the colour of the shading indicating the k-space velocity at that point. The top row shows trajectories which are spatially selective in a single direction and, consequently, much higher spatial frequencies are visited in that dimension.
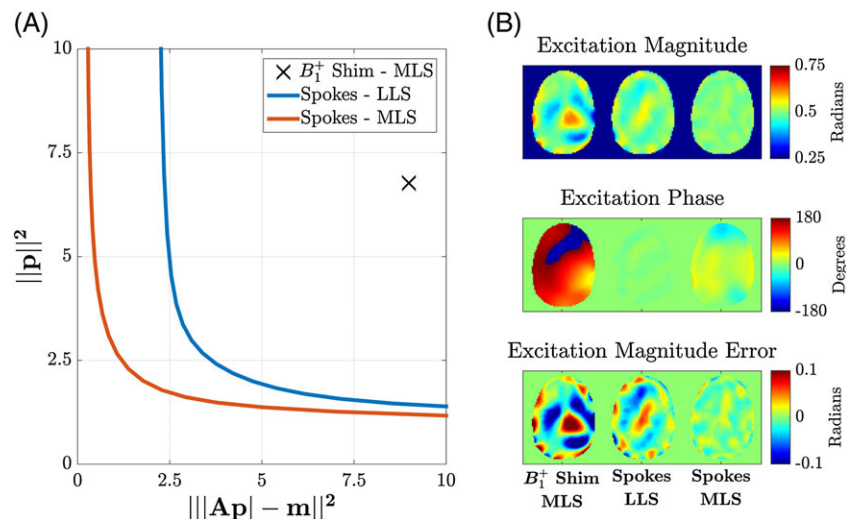
Figure 3. (A) L-curve showing the trade-off between power and homogeneity for a five-spoke flip angle shimming pulse solved using linear least squares (LLS) and magnitude least squares (MLS). The best MLS B_1^+ shimming result is also shown. (B) Excitation magnitudes (top), excitation phases (centre) and the magnitude error (bottom) with respect to the target excitation of 0.5. The displayed spokes solutions were chosen to have the same power as the best MLS B_1^+ shimming solution. (Data courtesy of Dr Alessandro Sbrizzi and Dr Hans Hoogduin, UMC Utrecht, the Netherlands.)

different regularisation parameters. The MLS B_1^+ shimming result is only able to produce a moderately uniform field. The LLS spokes method produces an excitation with a more uniform magnitude, but is constrained to produce uniform phase. The MLS spokes method produces the most uniform excitation by relaxing the phase constraint.

If spatial selectivity is not necessary, simple hard pulses are often employed (which correspond to a point at **k** = 0). Low-frequency k-space modulations can also be introduced in three dimensions; the k_T–points method is a direct generalisation of 2D spokes, with the trajectory 'stopping' at discrete locations in k-space (105). Alternatively, the 'spiral non-selective' (SPINS) method uses a continuously moving three-dimensional (3D) spiral trajectory to cover a low-frequency 3D k-space at variable velocity (106).

Flip angle shimming PTx pulses have been applied to both brain and body imaging. 2D spokes have been shown to improve 7T brain (66), cardiac (74) and liver (107) imaging. Figure 4 shows liver images obtained at 7 T using spokes pulses with increasing numbers of spokes – the achievable homogeneity increases at the expense of increasing pulse durations. 3D non-selective pulses have also been shown to benefit high-field brain imaging (108,109). Figure 5 shows magnetisation-prepared rapid gradient echo (MP-RAGE) images acquired using SPINS excitation pulses with a two-channel PTx system at 7 T. The relatively large amount of gradient encoding employed by SPINS pulses means that they can be effective with potentially a small number of transmit channels; at 3 T, good performance was demonstrated using only a single transmit channel (106).

Spatially and spectrally selective PTx pulses

Another application of dynamic PTx pulse design is to reduce the duration of very long pulses, such as those used for LEx. Indeed, this is one of the primary applications originally envisaged for PTx (17,18) because of the direct analogy with parallel imaging. LEx pulses are inherently lengthy, as their k-space trajectories must visit high spatial frequencies in order to restrict the excited magnetisation to a small area. PTx allows the excitation k-space to be undersampled, with multiple transmit channels used to avoid aliasing, as is the case for image encoding with parallel imaging. Acceleration of such pulses is important, not only in order to make them usable within rapid sequences, but also in order to reduce relaxation and off-resonance effects.

PTx–LEx pulses have been an active area of development since the first demonstrations of the technique in post-mortem animal models at 4.7 T (110) and in humans at 3 T (111). PTx–LEx used for the purpose of reduced FOV imaging has so far found limited applications, perhaps as reducing the number of measurements results in a loss of signal-to-noise ratio (SNR), and this approach directly competes with standard receive side parallel imaging. However, as with parallel imaging, performance could be expected to be improved with the increased SNR available with UHF MRI. PTx–LEx may prove to be particularly useful
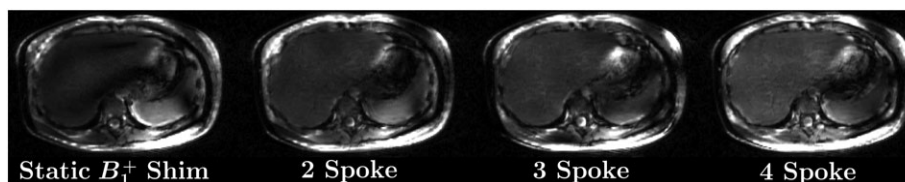
Figure 4. Liver imaging at 7 T with increasing numbers of spokes. Gradient echo images were each obtained within a single breath hold. In each case, homogeneity was optimised over the liver only and the images were processed to remove the receive field profiles. Homogeneity in the liver improves with an increasing number of spokes. (Images courtesy of Dr Xiaoping Wu, University of Minnesota, MN, USA, originally from Quant. Imaging Med. Surg. 2014; 4: 4–10, with permission.)

Quad. Excitation   SPINS
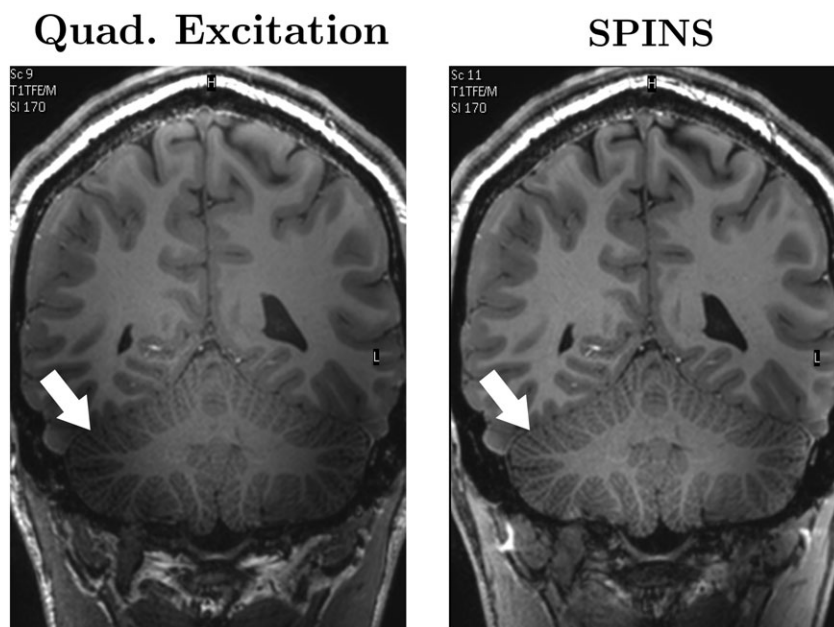
Figure 5. Matched coronal slices from T_1-weighted magnetisation-prepared rapid gradient echo (MP-RAGE) images acquired at 7 T using standard non-selective and spiral non-selective (SPINS) radiofrequency (RF) pulses with a two-channel head transmit coil. Both were acquired at an isotropic resolution of 0.8 mm with a flip angle of 8°, shot interval of 3.5 s, inversion delay of 1.2 s, TR = 9 ms, TE = 2.9 ms, parallel imaging reduction factors of 1.3x2 (anterior-posterior x right-left) with a total imaging time of approximately 10 minutes in both cases. Image uniformity was seen to have improved throughout the head, particularly in the cerebellum, as shown here. (Images courtesy of Dr Hans Hoogduin, UMC Utrecht, the Netherlands.)

in situations in which avoidance of artefacts is key, for example by not exciting moving structures, as demonstrated in rodents (112) and humans at 7 T (113,114). Another issue is that pulse durations, even after PTx acceleration, are typically still too long for use with rapid gradient echo or steady state free precession imaging sequences, but LEx may find a more natural use in other sequences, such as pulse-acquire spectroscopy, where TR is sufficiently long to tolerate a long RF pulse, or 3D fast spin echo (FSE) imaging, where only the excitation pulse needs to achieve spatial selectivity alongside subsequent non-selective refocusing pulses (115,116), as demonstrated in Fig. 6. Clinical implementations of PTX–LEx have also been demonstrated at 3 T, focusing on abdominal diffusion-weighted imaging applications where smaller FOVs can be used, reducing the length of the utilised echo planar imaging (EPI) readouts (117–119).

All RF pulses are spectrally selective to some degree, with bandwidth inversely related to duration; hence, typically, long LEx pulses tend to have narrow bandwidths. It is straightforward to add spectral selectivity to the Fourier STA approximation formalism as just another dimension whose associated 'k-space' variable is time (120). This property has long been exploited to produce spectral–spatial-selective pulses, such as binomial pulses often used for water or fat excitation. In fact, spokes pulses are identical in form to slice-selective spectral–spatial pulses with the addition of in-plane gradients. It has also been demonstrated that PTx can be used to achieve different excitation properties in water and fat, and to compensate for B_0 effects (121,122), within the same STA approximation design framework. With these methods, the additional degrees of freedom offered by PTx are being used to affect the spatial variation of the spectral response of the pulse by producing fields that are modulated in both space and time. If pulses are designed without accounting for frequency, they are in fact only controlling the on-resonance response. The inclusion of B_0 information in the

design process is successful for single chemical species materials; however, materials with different chemical shifts, such as fat, will have uncontrolled excitation properties. This can be remedied by solving over a range of frequencies (123) in order to extend the bandwidth, or indeed by solving only for particular frequencies of interest, such as water and fat (124).

There are many possible additional extensions to the spatial domain view of pulse design. For example, PTx has been employed to overcome EPI signal drop out present as a result of through-slice dephasing (125–127) by producing excitations that have the opposite phase variation through the slice and hence give refocused images at the echo time. Recent interest in the use of simultaneous multi-slice (SMS) excitations (128) with UHF MRI for ultra-high resolution diffusion and functional imaging (129) has also led to challenging pulse design problems as a result of the inherent high RF power and low bandwidth, in addition to B_1^+ inhomogeneity. Many methods incorporating SMS with PTx have been proposed and demonstrated at UHF (130–134), taking advantage of the distributed nature of PTx arrays to reduce peak RF power (a particular issue for SMS pulses), SAR and improve homogeneity. A recent study also proposed extending the spatial domain to include different 'virtual slices' that can be used to account for B_1^+ variation over the breathing cycle (135) – this approach extends the spatial domain to also include different respiratory phases, and improved robustness against respiration-induced errors was demonstrated.

k-space trajectory optimisation

The design methods outlined so far give an optimal RF waveform for a given trajectory, but, as only the resulting effect on the magnetisation is of any real importance, it would make more sense to consider the trajectory itself as also subject to optimisation. Unfortunately, although the RF design problem can be cast
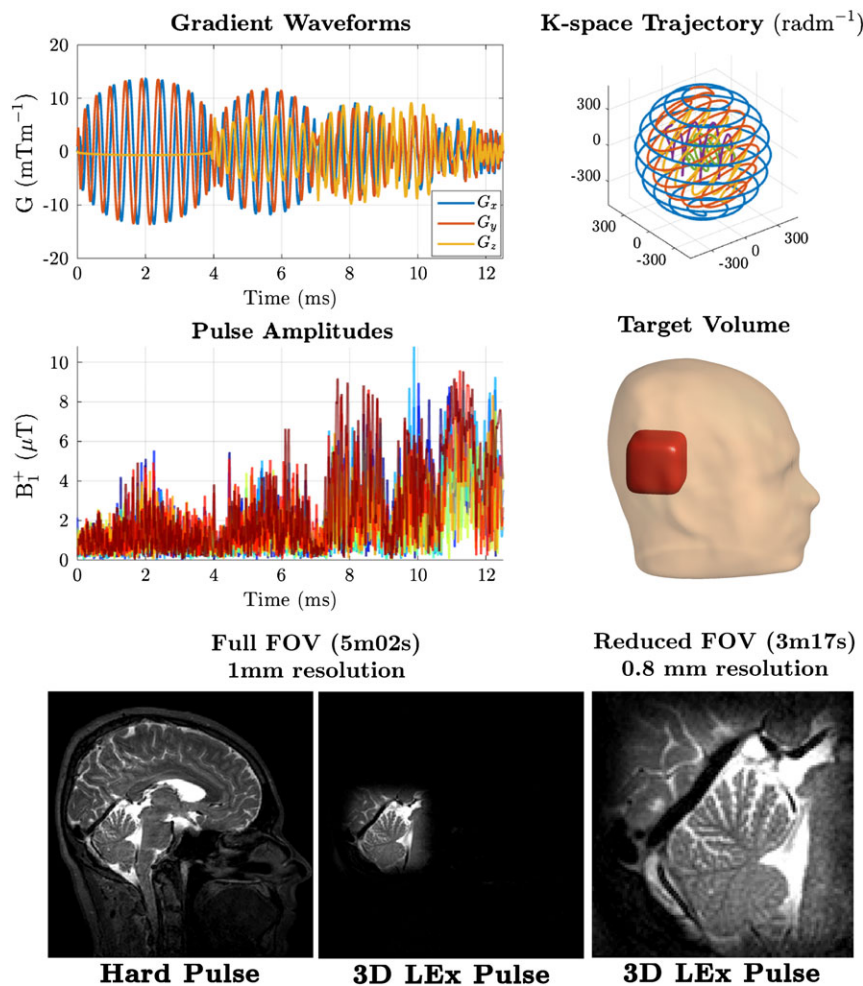
Figure 6. Three-dimensional eight-channel parallel transmission-local excitation (PTx-LEx) pulse design for three-dimensional (3D) fast spin echo imaging at 3 T (116). The gradient waveforms (top left) result in a 3D shells excitation k-space trajectory [top right, ref. (221)] consisting of multiple nested shells that are coloured separately here for clarity. The overall pulse duration is 12.3 ms. The pulses (middle left, different colours indicate different channels) are designed to produce a 90° excitation in the target volume placed over the cerebellum (middle right). Full field of view (FOV) image using non-selective hard pulse excitation (bottom left; isotropic resolution of 1 mm with parallel imaging reduction factors of 1.7x1.7 (anterior-posterior x right-left), full FOV image using designed LEx (bottom middle) and reduced FOV image using LEx (bottom right, isotropic resolution of 0.8 mm without parallel imaging).

straightforwardly as the inversion of a matrix problem, the trajectory enters into the design matrix itself, and therefore alternative methods are required to find both the optimal RF pulse and trajectory together.

A common approach is to create trajectories for classes of desired excitation pattern or for different RF coils that are manually or semi-automatically optimised. For example, SPINS pulses (106) were designed initially for inhomogeneity correction at 3 T, where the desired response is typically a dome shape in 3D; a low-frequency 3D spiral k-space trajectory is therefore a natural choice. The k-space locations for the rather simpler spokes (136) and k_T-points (105) trajectories are also often decided on the basis of similar arguments, for example using a 'Fourier' method that selects k-space locations which correspond to the highest energies in the Fourier transform of the target pattern.

A more rigorous strategy is to parameterise the trajectory and to formulate the pulse design problem as an optimisation over both the RF samples and trajectory parameters iteratively. This approach has been explored for 2D (137,138) and 3D (139) trajectories. Yip *et al.* (139) showed that this type of optimisation leads to intuitively reasonable results – for example, altering an

EPI trajectory to increase the sampling density in regions in which the Fourier transform of the target excitation has higher energy. A drawback is that the additional level of optimisation results in increased computation times, particularly as the trajectory optimisation is a non-linear problem. This issue is likely to be more significant for 3D problems, or when there are a large number of trajectory parameters, but simplifies when applied to spokes/k_T-points pulses. Zelinski *et al.* (140) showed that optimising by enforcing 'sparsity' of k-space locations helps to reduce the number of required spokes and performs better than the simple Fourier approach. The choice of multiple locations simultaneously is a computationally complex problem; Ma *et al.* (141) proposed a fast greedy algorithm which chooses locations one at a time, which reduces these requirements considerably. The frequency selectivity of the pulse is also determined by the time ordering of the locations chosen, and so an updated greedy algorithm was proposed to also take this into account (142).

As well as excitation fidelity, trajectories can also be optimised to minimise the required RF power. For example, spiral trajectories designed for 2D excitation have employed lower slew rates towards the centre of k-space (98,143) in order to reduce

instantaneous RF power, similar to applying variable rate selective excitation (VERSE) (144). An alternative solution is to numerically optimise a trajectory based on properties of the target (145,146). A more comprehensive approach for constraining peak instantaneous power was proposed by Lee *et al.* (147) who modified a time-optimal implementation of the VERSE algorithm (148) by transforming the constraint on peak RF power, so that it could be included as a gradient constraint. An issue with VERSE is that time dilating RF pulses changes their off-resonance properties. Lee *et al.* (149) proposed an updated version of their method which iteratively alters the RF design after time dilation to counter this issue.

Of the methods discussed so far, some update k-space on a per-subject basis (137,139,147,149), whereas others have a fixed trajectory (and hence gradient waveform) for all subjects (106,143,145,146). Although the latter group is less flexible, these methods do avoid the performance of additional calculations whilst the subject is *in situ*. Another advantage of this latter approach is that gradient system imperfections can be calibrated in advance. PTx pulses with complex gradient waveforms are often more sensitive than standard pulses to gradient system errors (150,151). In cases in which the waveforms do not change from subject to subject, these can be measured in advance with the true trajectory used for pulse design (106,152); this is feasible because the required corrections have been reported to remain stable over long periods of time (106). Methods that adapt trajectories for each subject may need to incorporate gradient imperfections using models, for example by treating them as a linear time-invariant system and employing an impulse response function (116,153,154). Waveform measurement using MRI and iterative predistortion (155) of waveforms require gradient measurements that can be performed quickly with the subject *in situ*; although image-based methods are available (for example, ref. (156)), this general approach is much more feasible if gradient probe measurements are available (157).

Beyond the STA approximation

The STA approximation provides an elegant Fourier picture which is useful for discussion as well as for simplifying the design problem. However, the linear k-space picture breaks down for large tip angles (LTAs) and, although some classes of k-space trajectory can produce satisfactory results (158), more sophisticated design methods are required. Non-PTx LTA pulse design can be performed using the Shinnar Le-Roux (SLR) algorithm (159,160), which was recently extended to multidimensional k-space trajectories (161). However, other methods are required for LTA PTx design; many approaches have been proposed, and these typically incorporate B_1^+ field information. A simple extension to STA approximation pulse design is the 'additive angle' method (162), which uses STA approximation designed iteratively with a Bloch simulation, designing a new pulse at each stage to compensate for the errors of the previous one, and then summing all of these contributions at the end. This method can be improved upon by performing a perturbation analysis of the Bloch equations; the STA approximation is the first-order term, but higher orders can be addressed iteratively to improve the design (163). These methods usually require multiple Bloch equation simulations to accurately model the magnetisation behaviour. The simplest case is that of 'composite' pulses, consisting of trains of a few non-selective pulses; the solution to the Bloch equations here can be boiled down to a set of simple rotations,

and these can be optimised numerically (164). More sophisticated pulses can be designed using optimal control methods, which solve dynamic optimisation problems with differential equations as constraints. These have a long history of use within MRI (for example, ref. (165)), and have been used recently for PTx RF pulse design (108,166–168), with much work carried out to reduce computation times and to find globally rather than locally optimal solutions.

Finally, the trend of parallelising the subsystems of MRI scanners has recently been extended to gradients. The parallel imaging technique using local gradients (PatLoc) (169) and O-space (170) imaging offer the ability to image higher resolutions with lower peripheral nerve stimulation (PNS) by using non-bijective gradients. PTx has been unified with these methods, but the Fourier domain picture does not apply because of the non-linearity of the spatial gradients (171).

MULTI-PULSE PTX

So far, the methods discussed have either fixed the B_1^+ field pattern throughout an RF pulse or modulated it over very short timescales, during a single RF pulse. An intermediate timescale also exists: modulation between pulses in one single sequence, referred to here as multi-pulse PTx. As discussed earlier, there is typically a trade-off between achievable B_1^+ homogeneity and RF power/SAR. One use for multi-pulse PTx is to apply this trade-off flexibly within a sequence. Homann *et al.* (172) proposed switching static PTx weights mid-scan between high SAR, good B_1^+ homogeneity settings when low-frequency k-space data are being acquired and low SAR, poor homogeneity settings when outer k-space data are being obtained. This minimises the impact of poor B_1^+ homogeneity on image contrast which is dominated by the RF conditions when acquiring the centre of k-space, whilst reducing the average SAR. Metzger *et al.* (90) used a similar principle for inversion-prepared renal angiography at 7 T; low SAR weights are used for adiabatic inversion pulses as these can tolerate some B_1^+ inhomogeneity, but typically have high associated SAR, whereas high B_1^+ homogeneity weights are used for excitation pulses whose homogeneity directly affects image quality, but which have a lower overall impact on the sequence SAR. A related method is time-interleaved acquisition of modes (TIAMO) (173,174), which can be used to remove signal voids caused by regions of low or even zero B_1^+ employing a parallel imaging reconstruction to create a composite image of data acquired using interleaved static PTx drives with different spatial sensitivity patterns that shift low B_1^+ areas to different locations.

By their nature, MRI pulse sequences consist of many RF pulses, and the overall effect on the received signal depends on the interactions between these pulses and the spin system. All of the RF pulse design and shimming strategies discussed so far have treated each pulse in isolation; however, an alternative is to take a more integrated approach. One example is to design pairs of pulses together, which can be beneficial in situations in which pulse properties need to be 'matched', as demonstrated for spin echo excitation and refocusing pulse pairs (175) and for flip-down/flip-up pairs (176).

In rapid imaging sequences, the magnetisation will reach a steady or pseudo-steady state (PSS) after many RF pulses; it has been shown that dynamic modulation of the static PTx weights during FSE sequences (177) can lead to better image quality than

static B_1^+ shimming alone. This approach, referred to here as direct signal control (DSC), is fundamentally different from those discussed so far. Although B_1^+ shimming typically seeks to control the B_1^+ field pattern, and flip angle shimming controls the transverse magnetisation at the end of an RF pulse, DSC may be thought of as 'signal shimming', where we seek to directly influence the signals that will be received during an imaging sequence consisting of multiple interacting RF pulses. One way of achieving this is by performing a non-linear optimisation with respect to a signal model; for FSE sequences, this can be efficiently constructed from a spatially resolved extension to the well-known extended phase graph (EPG) formalism (178). The method has been applied to 3D FSE imaging at 3 T (179), and related approaches which employ full PTx refocusing pulses have been demonstrated at 7 T (180–182), an example of which is illustrated in Fig. 7.

SAR

Increased SAR is intrinsically a problem for UHF MRI and is an area in which PTx can have both positive and negative effects. As PTx results in spatiotemporal variations in electric (as well as magnetic) RF fields, it can change the expected locations of hot spots. If local SAR is not considered when performing PTx calculations, a significant risk of heating can result. Global (i.e. whole body averaged) SAR can be estimated using measurements of forward and reflected power (183), but the estimation of local SAR typically requires a knowledge of electric fields. These cannot currently be measured reliably by MRI (although

it is an active research field (184–187)), and so this information is typically provided by numerically solving Maxwell's equations on a high-resolution grid (typically 1–5 mm^3) for digital body models. Once obtained, the *E*-field data can be related to SAR using the Q-matrix framework (188), which represents, in a matrix, the contribution to SAR from each possible combination of channels. For example, the instantaneous local SAR is given by Equation [5], where $\sigma(\mathbf{r})$ is the tissue conductivity, $\rho(\mathbf{r})$ is the tissue density and $\mathbf{Q}(\mathbf{r})$ is the Q-matrix at location $\mathbf{r}$. The global SAR matrix $\mathbf{Q}_{global}$ can be inferred by taking a weighted average of the local Q matrices (189).

$$SAR_{local}(\mathbf{r}) = \frac{\sigma(\mathbf{r})}{2\rho(\mathbf{r})} \mathbf{w}^{H} \mathbf{Q}(\mathbf{r}) \mathbf{w} \qquad [5]$$

All parts of the body exposed to the RF fields must be considered when evaluating SAR, not just those in the imaging region. As the location of maximum local SAR can occur anywhere and is not known a priori, Equation [5] must be evaluated for every location in space to ensure that regulatory limits are met. This is time consuming because of the sheer number of matrices, often in the range of 10^6–10^8. This process can be significantly accelerated by taking advantage of the positive semi-definite nature of the Q-matrices to form a smaller subset (known as 'virtual observation points') of Q-matrices, $\mathbf{Q}_{VOP}$, whose local SAR values dominate the calculation (190,191). Compression factors of the order of 5000 have been demonstrated for human models with eight transmit channels (190) with the guarantee of no
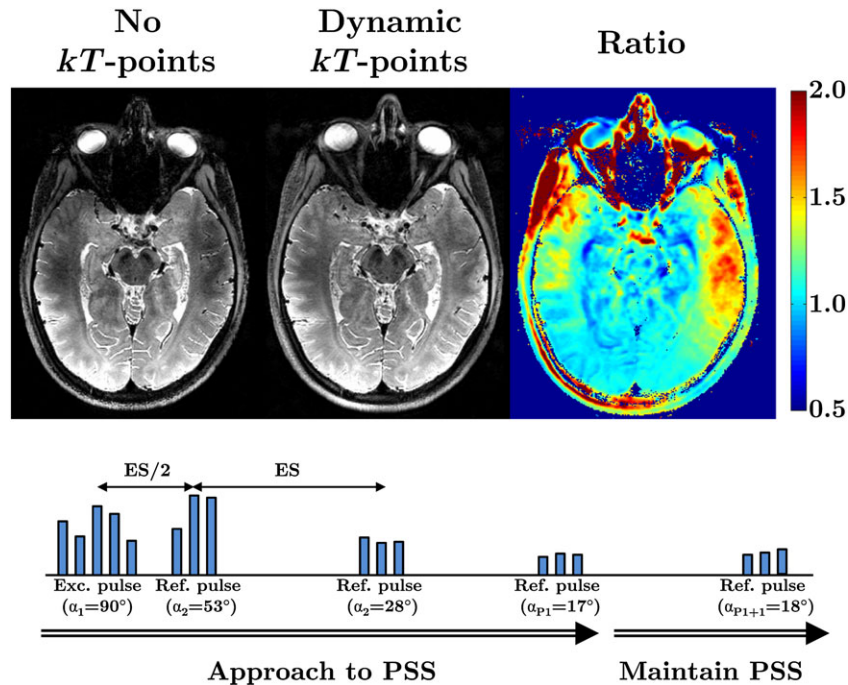
Figure 7. T_2-weighted three-dimensional fast spin echo (FSE) imaging at 7 T using dynamically modulated k_T-points radiofrequency (RF) pulses for excitation and refocusing. The diagram (bottom) depicts the k_T-points RF pulses used, consisting of multiple hard pulses. The amplitudes and phases of these hard pulses are optimised so that, during each shot of the FSE sequence, the magnetization is brought to a pseudo-steady state (PSS) with desired echo amplitude by the first P_1 pulse (here $P_1 = 10$), and then subsequently maintained in this state, despite the presence of strong B_1^+ non-uniformity. The spatially resolved extended phase graph (SR-EPG) framework is used to predict the echo amplitudes for all locations in space and at each TE, and these are optimized to be uniform (182). Dynamic modulation allows more uniform signals to be obtained, recovering reduced signals that are apparent in the temporal lobes (see increased signal apparent on the ratio image). (Images courtesy of Dr Florent Eggenschwiler, CIBM, Lausanne, Switzerland.)

underestimation of max{SAR$_{local}$} and a prescribed limit for over-estimation, in this case 5%.

Much work has gone into understanding the exact properties of the required digital body models (for example, ref. (192)). Many strategies have been proposed, including the production of patient-specific whole-body models based on *in situ* scans of a given subject (193), the creation of patient-specific models by image registration (194) or the use of generic models with a suitably chosen conservative safety factor (195). Although the majority of proposed methods rely on some form of SAR model, others are also exploring the possibility of direct *in vivo* measurement by post-processing B_1^+ maps, with results demonstrated at 3 T (196) and 7 T (185). Clearly, direct measurement of SAR would be ideal; however, these methods could only be practically used if the necessary data could be acquired quickly so as not to compromise the examination itself – this is made more challenging by the fact that areas of elevated SAR can occur far from the slice or volume that is being considered for imaging, and so SAR measurements will necessarily require large fields of view for many coil designs. Direct measurements of temperature increases are also being explored as a way of determining safe scanning using MR thermometry (187,197).

Once SAR information has been obtained, it can be used to limit SAR within pulse sequences (90,172,173). For PTx pulse designs, this is achieved by incorporating SAR penalisation terms into the cost functions minimised to calculate the pulse waveforms (e.g. Equations [2] and [4]). Table 2 describes the SAR terms commonly used in static PTx optimisation problems. All involve a quadratic form of the weights and Q-matrices. These terms can be easily generalised for dynamic PTx pulse calculations to limit local SAR (46,47). This type of constraint is useful, given that it has been shown that maximum local SAR, in particular, can vary strongly when pulse design parameters are changed (198). It has also been proposed that pulse design can be used to directly constrain temperature rather than SAR, by combining SAR models with biophysical thermal models utilising the Pennes bioheat equation (99).

Rather than viewing SAR as a constraint, the reduction of SAR can be seen as the major target of any optimisation – Zhu (18) discussed this possibility in his early paper on PTx, and it has been shown that simultaneous reductions in local SAR and B_1^+ inhomogeneity can be achieved by performing B_1^+ shimming within localised ROIs for prostate imaging at 7 T (34) and for cardiac imaging at 3 T (199). A further application of PTx has been the control and reduction of SAR in the presence of implanted or interventional devices (200–203). These methods use spatial control of RF electric fields, made possible by PTx, in order to minimise heating effects using simulated electric fields or *in situ* measurements of electrical coupling for optimisation. This is a promising application for PTx that has so far been of particular interest at lower field strengths.

Finally, it should also be noted that electric fields and SAR depend on the utilised RF coil. It has been shown that certain transmit arrays can be driven using a basis of circularly polarised modes (204), some of which produce very little B_1^+ yet significant electric fields. Although they produce very little B_1^+, these 'dark modes' can be used to cancel electric fields produced by the more B_1^+ efficient modes to reduce SAR hotspots (205). Taking this concept further, it is possible to design coil arrays with some dedicated 'dark' elements that primarily produce electric fields. An example of such a system is illustrated in Fig. 8 from ref. (206), where dipole antennas are employed in conjunction with loops. Although this design is unconventional, each element in this array is driven independently, and it may be used in exactly the same way as any other PTx array using any of the optimization methods outlined previously. It has been demonstrated that potentially large reductions in local SAR (206) can be achieved. Although these approaches are still in their infancy, previous theoretical studies into optimal current distributions suggest that there are significant benefits yet to be obtained (61,207).

B_1^+ MAPPING

PTx methods inherently require some knowledge of the transmit field produced by each element of the transmit array. This information is typically acquired *in situ*, and many different strategies have been proposed. The most basic approach involves the utilisation of a sequence which measures the magnitude of the transmit field (for example, see refs. (208–211)), and repeating this for each transmitter. The relative phase of each transmitter is either obtained from the phase of the images acquired or, in some cases, from a dedicated acquisition (212). This approach is typically lengthy, as the majority of B_1^+ mapping methods (apart from recently proposed exceptions (211–213)) are slow and, unlike receive field mapping, transmit channels must be mapped sequentially. Another approach is to acquire only a single magnitude transmit field map of all coils transmitting in a default configuration, supplemented by a series of low-flip-angle spoiled gradient echo images (214,215) (whose signal is proportional to the B_1^+ field) from which relative transmitter information can be obtained. This technique is fast, as the data acquisition is very efficient with low SAR.

UHF B_1^+ mapping is more challenging than at lower field strengths, primarily because of the increased dynamic range of the transmit field; typically very large B_1^+ is produced adjacent to coil elements, with very low and often zero amplitudes produced further away within the FOV. All B_1^+ mapping methods have a limited range of flip angles over which they can acquire accurate measurements (216). In order to combat this, the use of linear combinations (LCs), constructed so as to reduce the dynamic range, has been proposed (217,218). The choice of LC usually requires a trade-off between reducing the dynamic range and the ability to invert the measurements (219). Recent work at 9.4 T has suggested that Fourier encoding is a good choice using an eight-channel head coil (220), but work at 3 T has shown that the best choice of LC is coil array and load specific (219), and a suitable LC cannot always be found.

Table 2. Example cost function terms Φ_{SAR} used to constrain the specific absorption rate (SAR) in static parallel transmission (PTx) optimisation problems

Energy constraints	Cost function term	References
Total RF power (**I**, identity matrix)	$\mathbf{w}^H \mathbf{I} \mathbf{w}$	(92)
Global SAR	$\mathbf{w}^H \mathbf{Q}_{global} \mathbf{w}$	(18)
Local SAR (index *i* runs over all spatial locations)	$\mathbf{w}^H \mathbf{Q}(\mathbf{r}_i) \mathbf{w} \; \forall \, i$	(46)
VOP SAR (index *i* runs over all VOPs)	$\mathbf{w}^H \mathbf{Q}_i^{VOP} \mathbf{w} \; \forall \, i$	(191,192)

MLS B_1^+ Shimming Results
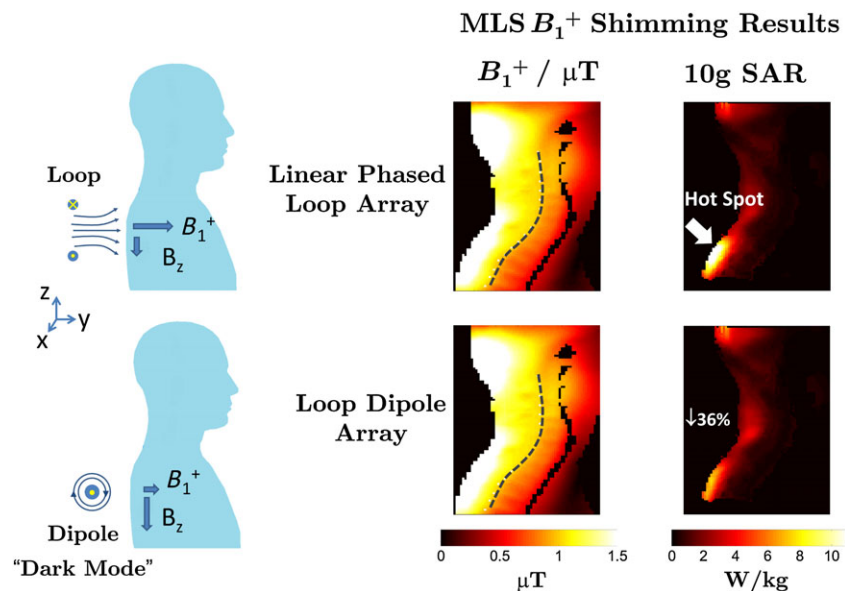
Figure 8. Specific absorption rate (SAR) reduction achieved by combining a loop and dipole array. The dipoles are orthogonal to the main magnetic field (*z*-axis), and therefore produce radiofrequency (RF) magnetic fields primarily in the *z*-axis – these produce very little contribution to the NMR and are hence referred to as 'dark modes'. The electric fields produced by the dipoles can, however, be used to cancel those produced by the loops, thus reducing local SAR. In this example, magnitude least squares (MLS) B_1^+ shimming using an array of four loops and four dipoles was able to reduce peak 10 gram SAR by 36% when compared with a four-loop linear phased array, whilst producing an almost identical B_1^+. (Images courtesy of Dr Yigitcan Eryaman, University of Minnesota, MN, USA. Data reproduced from Magn. Reson. Med, Epub 2014, doi: 10.1002/mrm.25246., with permission).

CONCLUDING REMARKS

UHF MRI provides a powerful tool for investigation of the human body, for both clinical diagnosis and fundamental research. However, it brings a new set of challenges which need to be overcome. This review has focused on how the new degrees of freedom made possible by PTx can be used, focusing on different temporal scales over which RF fields can be modulated and different ways in which this interacts with MR image formation. We have touched upon some of the remaining technical challenges, such as accurate estimation of SAR and rapid B_1^+ mapping, but there are also additional RF engineering issues, such as optimal design of RF coils and amplifiers, that are beyond the scope of this review. Many of the methods discussed here have been proposed in methodological studies, but as PTx technology matures and becomes more widespread for UHF MRI, it is hoped that some will now prove their efficacy for routine *in vivo* research and clinical use.

Acknowledgements

REFERENCES

1. Röschmann P. Radiofrequency penetration and absorption in the human body: limitations to high-field whole-body nuclear magnetic resonance imaging. Med. Phys. 1987; 14: 922–931.
2. Ibrahim TS, Lee R, Abduljalil AM, Baertlein BA, Robitaille P-ML. Dielectric resonances and B_1 field inhomogeneity in UHFMRI: computational analysis and experimental findings. Magn. Reson. Imaging 2001; 19: 219–226.
3. Ibrahim TS, Hue Y-K, Tang L. Understanding and manipulating the RF fields at high field MRI. NMR Biomed. 2009; 22: 927–936.
4. Van de Moortele PF, Akgun C, Adriany G, Moeller S, Ritter J, Collins CM, Smith MB, Vaughan JT, Uğurbil K. B_1 destructive interferences and spatial phase patterns at 7 T with a head transceiver array coil. Magn. Reson. Med. 2005; 54: 1503–1518.
5. Wiesinger F, Van de Moortele PF, Adriany G, De Zanche N, Ugurbil K, Pruessmann KP. Parallel imaging performance as a function of field strength—an experimental investigation using electrodynamic scaling. Magn. Reson. Med. 2004; 52: 953–964.
6. Wiesinger F, Boesiger P, Pruessmann KP. Electrodynamics and ultimate SNR in parallel MR imaging. Magn. Reson. Med. 2004; 52: 376–390.
7. Liu W, Collins C, Smith M. Calculations of B_1^+ distribution, specific energy absorption rate, and intrinsic signal-to-noise ratio for a body-size birdcage coil loaded with different human subjects at 64 and 128 MHz. Appl. Magn. Reson. 2005; 29: 5–18.
8. Norris DG. Adiabatic radiofrequency pulse forms in biomedical nuclear magnetic resonance. Concepts Magn. Reson. 2002; 14: 89–101.
9. Balchandani P, Glover G, Pauly J, Spielman D. Improved slice-selective adiabatic excitation. Magn. Reson. Med. 2014; 71: 75–82.
10. Schmitt M, Feiweier T, Horger W, Krueger G, Schoen L, Lazar R, Kiefer B. Improved uniformity of RF-distribution in clinical whole body imaging at 3 T by means of dielectric pads. *Proceedings of the 12th Annual Meeting ISMRM*, Kyoto, Japan, 2004; 197.
11. Yang QX, Mao W, Wang J, Smith MB, Lei H, Zhang X, Ugurbil K, Chen W. Manipulation of image intensity distribution at 7.0 T: passive RF shimming and focusing with dielectric materials. J. Magn. Reson. Imaging 2006; 24: 197–202.
12. Webb AG. Dielectric materials in magnetic resonance. Concepts Magn. Reson. Part A 2011; 38A: 148–184.

13. Alsop DC, Connick TJ, Mizsei G. A spiral volume coil for improved RF field homogeneity at high static magnetic field strength. Magn. Reson. Med. 1998; 40: 49–54.

14. Vaughan JT, Hetherington HP, Otu JO, Pan JW, Pohost GM. High frequency volume coils for clinical NMR imaging and spectroscopy. Magn. Reson. Med. 1994; 32: 206–218.

15. Hoult DI. Sensitivity and power deposition in a high-field imaging experiment. J. Magn. Reson. Imaging 2000; 12: 46–67.

16. Ibrahim TS, Lee R, Baertlein BA, Kangarlu A, Robitaille P-ML. Application of finite difference time domain method for the design of birdcage RF head coils using multi-port excitations. Magn. Reson. Imaging 2000; 18: 733–742.

17. Katscher U, Börnert P, Leussler C, Van den Brink JS. Transmit SENSE. Magn. Reson. Med. 2003; 49: 144–150.

18. Zhu Y. Parallel excitation with an array of transmit coils. Magn. Reson. Med. 2004; 51: 775–784.

19. Shajan G, Hoffmann J, Budde J, Adriany G, Ugurbil K, Pohmann R. Design and evaluation of an RF front-end for 9.4 T human MRI. Magn. Reson. Med. 2011; 66: 594–602.

20. Hoult DI, Kolansky G, Kripiakevich D, King SB. The NMR multitransmit phased array: a Cartesian feedback approach. J. Magn. Reson. 2004; 171: 64–70.

21. Stang PP, Conolly SM, Santos JM, Pauly JM, Scott GC. Medusa: a scalable MR console using USB. IEEE Trans. Med. Imaging 2012; 31: 370–379.

22. Gudino N, Heilman JA, Riffe MJ, Heid O, Vester M, Griswold MA. On-coil multiple channel transmit system based on class-D amplification and pre-amplification with current amplitude feedback. Magn. Reson. Med. 2013; 70: 276–289.

23. Chu X, Yang X, Liu Y, Sabate J, Zhu Y. Ultra-low output impedance RF power amplifier for parallel excitation. Magn. Reson. Med. 2009; 61: 952–961.

24. Hoult DI. The principle of reciprocity in signal strength calculations—a mathematical guide. Concepts Magn. Reson. 2000; 12: 173–187.

25. Collins CM, Wang Z. Calculation of radiofrequency electromagnetic fields and their effects in MRI of human subjects. Magn. Reson. Med. 2011; 65: 1470–1482.

26. International Electrotechnical Commission (IEC). *Medical electrical equipment - Part 2-33: Particular requirements for the basic safety and essential performance of magnetic resonance equipment for medical diagnosis (IEC-60601-2-33)*. IEC: Geneva; 2010.

27. Ibrahim TS, Lee R, Baertlein BA, Abduljalil AM, Zhu H, Robitaille P-ML. Effect of RF coil excitation on field inhomogeneity at ultra high fields: a field optimized TEM resonator. Magn. Reson. Imaging 2001; 19: 1339–1347.

28. Wang ZJ, Chu Z. Achieving plane-wise uniform B_1 amplitude in a 3D volume for high-field MRI: a computer simulation study. J. Magn. Reson. Imaging 2006; 24: 218–225.

29. Mao W, Smith MB, Collins CM. Exploring the limits of RF shimming for high-field MRI of the human head. Magn. Reson. Med. 2006; 56: 918–922.

30. Seifert F, Rinneberg H. Adaptive coil control: SNR optimization of a TR volume coil for single voxel MRS at 3 T. *Proceedings of the 10th Annual Meeting ISMRM*, Honolulu, HI, USA, 2002; 162.

31. Vaughan JT, Adriany G, Snyder CJ, Tian J, Thiel T, Bolinger L, Liu H, DelaBarre L, Ugurbil K. Efficient high-frequency body coil for high-field MRI. Magn. Reson. Med. 2004; 52: 851–859.

32. Adriany G, Van de Moortele PF, Wiesinger F, Moeller S, Strupp JP, Andersen P, Snyder C, Zhang X, Chen W, Pruessmann KP, Boesiger P, Vaughan T, Uğurbil K. Transmit and receive transmission line arrays for 7 Tesla parallel imaging. Magn. Reson. Med. 2005; 53: 434–445.

33. Vaughan T, DelaBarre L, Snyder C, Tian J, Akgun C, Shrivastava D, Liu W, Olson C, Adriany G, Strupp J, Andersen P, Gopinath A, Van de Moortele PF, Garwood M, Ugurbil K. 9.4 T human MRI: preliminary results. Magn. Reson. Med. 2006; 56: 1274–1282.

34. Van den Bergen B, Van den Berg CAT, Bartels LW, Lagendijk JJW. 7 T body MRI: B_1 shimming with simultaneous SAR reduction. Phys. Med. Biol. 2007; 52: 5429–5441.

35. Metzger GJ, Snyder C, Akgun C, Vaughan T, Ugurbil K, Van de Moortele PF. Local B_1^+ shimming for prostate imaging with transceiver arrays at 7 T based on subject-dependent transmit phase measurements. Magn. Reson. Med. 2008; 59: 396–409.

36. Katscher U, Vernickel P, Graesslin I, Börnert P. RF shimming using a multi-element transmit system in phantom and in vivo studies. *Proceedings of the Joint Annual Meeting ISMRM-ESMRMB*, Berlin, Germany, 2007; 1693.

37. Kerr AB, Zhu Y, Pauly JM. Phase constraint relaxation in parallel excitation pulse design. *Proceedings of the Joint Annual Meeting ISMRM-ESMRMB*, Berlin, Germany, 2007; 1694.

38. Setsompop K, Wald LL, Alagappan V, Gagoski BA, Adalsteinsson E. Magnitude least squares optimization for parallel radio frequency excitation design demonstrated at 7 Tesla with eight channels. Magn. Reson. Med. 2008; 59: 908–915.

39. Setsompop K, Wald LL, Adalsteinsson E. Reduced-voltage RF shimming for adiabatic pulse design in parallel transmission. *Proceedings of the Joint Annual Meeting ISMRM-ESMRMB*, Berlin, Germany, 2007; 1687.

40. Balchandani P, Khalighi MM, Hsieh SS, Setsompop K, Pauly J, Spielman D. Adiabatic B_1 shimming algorithm for multiple channel transmit at 7 T. *Proceedings of the 19th Annual Meeting ISMRM*, Montreal, QC, Canada, 2011; 2907.

41. Deniz CM, Brown R, Lattanzi R, Alon L, Sodickson DK, Zhu Y. Maximum efficiency radiofrequency shimming: theory and initial application for hip imaging at 7 tesla. Magn. Reson. Med. 2013; 69: 1379–1388.

42. Ibrahim TS. Ultrahigh-field MRI whole-slice and localized RF field excitations using the same RF transmit array. IEEE Trans. Med. Imaging 2006; 25: 1341–1347.

43. Abraham R, Ibrahim TS. Proposed radiofrequency phased-array excitation scheme for homogenous and localized 7-Tesla whole-body imaging based on full-wave numerical simulations. Magn. Reson. Med. 2007; 57: 235–242.

44. Olson C, Yoo H, Delabarre L, Vaughan JT, Gopinath A. RF B_1 field localization through convex optimization. Microw. Opt. Technol. Lett. 2012; 54: 31–37.

45. Yoo H, Gopinath A, Vaughan JT. A method to localize RF field in high-field magnetic resonance imaging systems. IEEE Trans. Biomed. Eng. 2012; 59: 3365–3371.

46. Brunner DO, Pruessmann KP. Optimal design of multiple-channel RF pulses under strict power and SAR constraints. Magn. Reson. Med. 2010; 63: 1280–1291.

47. Guérin B, Gebhardt M, Cauley S, Adalsteinsson E, Wald LL. Local specific absorption rate (SAR), global SAR, transmitter power, and excitation accuracy trade-offs in low flip-angle parallel transmit pulse design. Magn. Reson. Med. 2014; 71: 1446–1457.

48. Grissom WA, Kerr AB, Stang P, Scott GC, Pauly JM. Minimum envelope roughness pulse design for reduced amplifier distortion in parallel excitation. Magn. Reson. Med. 2010; 64: 1432–1439.

49. Raaijmakers AJE, Ipek O, Klomp DWJ, Possanzini C, Harvey PR, Lagendijk JJW, Van den Berg CAT. Design of a radiative surface coil array element at 7 T: the single-side adapted dipole antenna. Magn. Reson. Med. 2011; 66: 1488–1497.

50. Willinek WA, Gieseke J, Kukuk GM, Nelles M, König R, Morakkabati-Spitz N, Träber F, Thomas D, Kuhl CK, Schild HH. Dual-source parallel radiofrequency excitation body MR imaging compared with standard MR imaging at 3.0 T: initial clinical experience. Radiology 2010; 256: 966–975.

51. Nelles M, König RS, Gieseke J, Guerand-van Battum MM, Kukuk GM, Schild HH, Willinek WA. Dual-source parallel RF transmission for clinical MR imaging of the spine at 3.0 T: intraindividual comparison with conventional single-source transmission. Radiology 2010; 257: 743–753.

52. Kukuk GM, Gieseke J, Weber S, Hadizadeh DR, Nelles M, Träber F, Schild HH, Willinek WA. Focal liver lesions at 3.0 T: lesion detectability and image quality with T2-weighted imaging by using conventional and dual-source parallel radiofrequency transmission. Radiology, 2011; 259: 421–428.

53. Rahbar H, Partridge SC, DeMartini WB, Gutierrez RL, Parsian S, Lehman CD. Improved B_1 homogeneity of 3 tesla breast MRI using dual-source parallel radiofrequency excitation. J. Magn. Reson. Imaging 2012; 35: 1222–1226.

54. Mürtz P, Kaschner M, Träber F, Kukuk GM, Büdenbender SM, Skowasch D, Gieseke J, Schild HH, Willinek WA. Evaluation of dual-source parallel RF excitation for diffusion-weighted whole-body MR imaging with background body signal suppression at 3.0 T. Eur. J. Radiol. 2012; 81: 3614–3623.

55. Pazahr S, Fischer MA, Chuck N, Luechinger R, Schick F, Nanz D, Boss A. Liver: segment-specific analysis of B_1 field homogeneity at 3.0-T

1157

MR imaging with single-source versus dual-source parallel radiofrequency excitation. Radiology 2012; 265: 591–599.

56. Trop I, Gilbert G, Ivancevic MK, Beaudoin G. Breast MR imaging at 3 T with dual-source radiofrequency transmission offers superior B_1 homogeneity: an intraindividual comparison with breast MR imaging at 1.5 T. Radiology 2013; 267: 602–608.

57. Krishnamurthy R, Pednekar A, Kouwenhoven M, Cheong B, Muthupillai R. Evaluation of a subject specific dual-transmit approach for improving B_1 field homogeneity in cardiovascular magnetic resonance at 3 T. J. Cardiovasc. Magn. Reson. 2013; 15: 68.

58. Bachschmidt TJ, Köhler M, Nistler J, Geppert C, Jakob PM, Nittka M. Polarized multichannel transmit MRI to reduce shading near metal implants. Magn. Reson. Med. 2015.

59. Childs AS, Malik SJ, O'Regan DP, Hajnal JV. Impact of number of channels on RF shimming at 3 T. Magn. Reson. Mater. Phys. Biol. Med. 2013; 26: 401–410.

60. Guérin B, Gebhardt M, Serano P, Adalsteinsson E, Hamm M, Pfeuffer J, Nistler J, Wald LL. Comparison of simulated parallel transmit body arrays at 3 T using excitation uniformity, global SAR, local SAR, and power efficiency metrics. Magn. Reson. Med. 2015; 73: 1137–1150.

61. Lattanzi R, Sodickson DK, Grant AK, Zhu Y. Electrodynamic constraints on homogeneity and radiofrequency power deposition in multiple coil excitations. Magn. Reson. Med. 2009; 61: 315–334.

62. De Martino F, Schmitter S, Moerel M, Tian J, Ugurbil K, Formisano E, Yacoub E, Van de Moortele PF. Spin echo functional MRI in bilateral auditory cortices at 7 T: an application of B_1 shimming. Neuroimage 2012; 63: 1313–1320.

63. Curtis AT, Gilbert KM, Klassen LM, Gati JS, Menon RS. Slice-by-slice B_1^+ shimming at 7 T. Magn. Reson. Med. 2012; 68: 1109–1116.

64. Gilbert KM, Curtis AT, Gati JS, Klassen LM, Menon RS. A radiofrequency coil to facilitate B_1^+ shimming and parallel imaging acceleration in three dimensions at 7 T. NMR Biomed. 2011; 24: 815–823.

65. Schmitter S, Wu X, Adriany G, Auerbach EJ, Uğurbil K, Van de Moortele PF. Cerebral TOF angiography at 7 T: impact of B_1^+ shimming with a 16-channel transceiver array. Magn. Reson. Med. 2014; 71: 966–977.

66. Schmitter S, Wu X, Auerbach EJ, Adriany G, Pfeuffer J, Hamm M, Uğurbil K, van de Moortele PF. Seven-Tesla time-of-flight angiography using a 16-channel parallel transmit system with power-constrained 3-dimensional spoke radiofrequency pulse design. Invest. Radiol. 2014; 49: 314–325.

67. Hoffmann J, Shajan G, Scheffler K, Pohmann R. Numerical and experimental evaluation of RF shimming in the human brain at 9.4 T using a dual-row transmit array. Magn. Reson. Mater. Phys. Biol. Med. 2014; 27: 373–386.

68. Budde J, Shajan G, Scheffler K, Pohmann R. Ultra-high resolution imaging of the human brain using acquisition-weighted imaging at 9.4 T. Neuroimage 2014; 86: 592–598.

69. Shajan G, Kozlov M, Hoffmann J, Turner R, Scheffler K, Pohmann R. A 16-channel dual-row transmit array in combination with a 31-element receive array for human brain imaging at 9.4 T. Magn. Reson. Med. 2014; 71: 870–879.

70. Boer VO, Klomp DWJ, Juchem C, Luijten PR, de Graaf RA. Multislice ^{1}H MRSI of the human brain at 7 T using dynamic B_0 and B_1 shimming. Magn. Reson. Med. 2012; 68: 662–670.

71. Hetherington HP, Avdievich NI, Kuznetsov AM, Pan JW. RF shimming for spectroscopic localization in the human brain at 7 T. Magn. Reson. Med. 2010; 63: 9–19.

72. Emir UE, Auerbach EJ, Van de Moortele PF, Marjańska M, Uğurbil K, Terpstra M, Tkáč I, Öz G. Regional neurochemical profiles in the human brain measured by ^{1}H MRS at 7 T using local B_1 shimming. NMR Biomed. 2012; 25: 152–160.

73. Deelchand DK, Van de Moortele PF, Adriany G, Iltis I, Andersen P, Strupp JP, Vaughan TJ, Uğurbil K, Henry PG. In vivo ^{1}H NMR spectroscopy of the human brain at 9.4 T: initial results. J. Magn. Reson. 2010; 206: 74–80.

74. Schmitter S, DelaBarre L, Wu X, Greiser A, Wang D, Auerbach EJ, Vaughan JT, Uğurbil K, Van de Moortele PF. Cardiac imaging at 7 tesla: single- and two-spoke radiofrequency pulse design with 16-channel parallel excitation. Magn. Reson. Med. 2013; 70: 1210–1219.

75. Hess AT, Bissell MM, Ntusi NAB, Lewis AJM, Tunnicliffe EM, Greiser A, Stalder AF, Francis JM, Myerson SG, Neubauer S, Robson MD. Aortic 4D flow: quantification of signal-to-noise ratio as a function of field strength and contrast enhancement for 1.5 T, 3 T, and 7 T. Magn. Reson. Med. 2015; 73: 1864–1871.

76. Suttie JJ, DelaBarre L, Pitcher A, Van de Moortele PF, Dass S, Snyder CJ, Francis JM, Metzger GJ, Weale P, Ugurbil K, Neubauer S, Robson MD, Vaughan JT. 7 Tesla (T) human cardiovascular magnetic resonance imaging using FLASH and SSFP to assess cardiac function: validation against 1.5 T and 3 T. NMR Biomed. 2012; 25: 27–34.

77. Snyder CJ, DelaBarre L, Metzger GJ, Van de Moortele PF, Akgun C, Ugurbil K, Vaughan JT. Initial results of cardiac imaging at 7 tesla. Magn. Reson. Med. 2009; 61: 517–524.

78. Rodgers CT, Piechnik SK, DelaBarre LJ, Van de Moortele PF, Snyder CJ, Neubauer S, Robson MD, Vaughan JT. Inversion recovery at 7 T in the human myocardium: measurement of T1, inversion efficiency and B_1^+. Magn. Reson. Med. 2013; 70: 1038–1046.

79. Tao Y, Hess AT, Keith GA, Rodgers CT, Liu A, Francis JM, Neubauer S, Robson MD. Optimized saturation pulse train for human first-pass myocardial perfusion imaging at 7 T. Magn. Reson. Med. 2015; 73: 1450–1456

80. Chang G, Deniz CM, Honig S, Egol K, Regatte RR, Zhu Y, Sodickson DK, Brown R. MRI of the hip at 7 T: feasibility of bone microarchitecture, high-resolution cartilage, and clinical imaging. J. Magn. Reson. Imaging 2014; 39: 1384–1393.

81. Ellermann J, Goerke U, Morgan P, Ugurbil K, Tian J, Schmitter S, Vaughan T, Van de Moortele PF. Simultaneous bilateral hip joint imaging at 7 Tesla using fast transmit B_1 shimming methods and multichannel transmission – a feasibility study. NMR Biomed. 2012; 25: 1202–1208.

82. Brown R, Deniz CM, Zhang B, Chang G, Sodickson DK, Wiggins GC. Design and application of combined 8-channel transmit and 10-channel receive arrays and radiofrequency shimming for 7-T shoulder magnetic resonance imaging. Invest. Radiol. 2014; 49: 35–47.

83. Zhao W, Cohen-Adad J, Polimeni JR, Keil B, Guerin B, Setsompop K, Serano P, Mareyam A, Hoecht P, Wald LL. Nineteen-channel receive array and four-channel transmit array coil for cervical spinal cord imaging at 7 T. Magn. Reson. Med. 2014; 72: 291–300.

84. Van den Bergen B, Klomp DWJ, Raaijmakers AJE, de Castro CA, Boer VO, Kroeze H, Luijten PR, Lagendijk JJW, Van den Berg CAT. Uniform prostate imaging and spectroscopy at 7 T: comparison between a microstrip array and an endorectal coil. NMR Biomed. 2011; 24: 358–365.

85. Metzger GJ, Van De Moortele PF, Akgun C, Snyder CJ, Moeller S, Strupp J, Andersen P, Shrivastava D, Vaughan JT, Ugurbil K, Adriany G. Performance of external and internal coil configurations for prostate investigations at 7 T. Magn. Reson. Med. 2010; 64: 1625–1639.

86. Maas MC, Vos EK, Lagemaat MW, Bitz AK, Orzada S, Kobus T, Kraff O, Maderwald S, Ladd ME, Scheenen TWJ. Feasibility of T2-weighted turbo spin echo imaging of the human prostate at 7 tesla. Magn. Reson. Med. 2014; 71: 1711–1719.

87. Fischer A, Kraff O, Maderwald S, Beiderwellen K, Ladd ME, Forsting M, Lauenstein TC, Umutlu L. Non-enhanced T1-weighted liver vessel imaging at 7 Tesla. PLoS One, 2014; 9: e97465.

88. Umutlu L, Kraff O, Orzada S, Fischer A, Kinner S, Maderwald S, Antoch G, Quick HH, Forsting M, Ladd ME, Lauenstein TC. Dynamic contrast-enhanced renal MRI at 7 Tesla: preliminary results. Invest. Radiol. 2011; 46: 425–433.

89. Umutlu L, Maderwald S, Kraff O, Kinner S, Schaefer LC, Wrede K, Antoch G, Forsting M, Ladd ME, Lauenstein TC, Quick HH. New look at renal vasculature: 7 tesla nonenhanced T1-weighted FLASH imaging. J. Magn. Reson. Imaging 2012; 36: 714–721.

90. Metzger GJ, Auerbach EJ, Akgun C, Simonson J, Bi X, Uğurbil K, Van de Moortele PF. Dynamically applied B_1^+ shimming solutions for non-contrast enhanced renal angiography at 7.0 tesla. Magn. Reson. Med. 2013; 69: 114–126.

91. Pauly J, Nishimura D, Macovski A. A k-space analysis of small-tip-angle excitation. J. Magn. Reson. 1989; 81: 43–56.

92. Grissom W, Yip C, Zhang Z, Stenger VA, Fessler JA, Noll DC. Spatial domain method for the design of RF pulses in multicoil parallel excitation. Magn. Reson. Med. 2006; 56: 620–629.

93. Zelinski AC, Wald LL, Setsompop K, Alagappan V, Gagoski BA, Goyal VK, Hebrank F, Fontius U, Schmitt F, Adalsteinsson E. Comparison of three algorithms for solving linearized systems of parallel excitation RF waveform design equations: experiments on an eight-channel system at 3 Tesla. Concepts Magn. Reson. Part B Magn. Reson. Eng. 2007; 31B: 176–190.

94. Yip C, Fessler JA, Noll DC. Advanced three-dimensional tailored RF pulse for signal recovery in T2*-weighted functional magnetic resonance imaging. Magn. Reson. Med. 2006; 56: 1050–1059.

95. Cloos MA, Luong M, Ferrand G, Amadon A, Le Bihan D, Boulant N. Local SAR reduction in parallel excitation based on channel-dependent Tikhonov parameters. J. Magn. Reson. Imaging 2010; 32: 1209–1216.

96. Wu X, Akgün C, Vaughan JT, Andersen P, Strupp J, Uğurbil K, Moortele PF. Adapted RF pulse design for SAR reduction in parallel excitation with experimental verification at 9.4 T. J. Magn. Reson. 2010; 205: 161–170.

97. Deniz CM, Alon L, Brown R, Sodickson DK, Zhu Y. Specific absorption rate benefits of including measured electric field interactions in parallel excitation pulse design. Magn. Reson. Med. 2012; 67: 164–174.

98. Graesslin I, Biederer S, Schweser F, Zimmermann KH, Katscher U, Börnert P. SAR reduction for parallel transmission using VERSE and k-space filtering. Proceedings of the Joint Annual Meeting ISMRM-ESMRMB, Berlin, Germany, 2007; 674.

99. Boulant N, Massire A, Amadon A, Vignaud A. Radiofrequency pulse design in parallel transmission under strict temperature constraints. Magn. Reson. Med. 2014; 72: 679–688.

100. Deichmann R, Good CD, Turner R. RF inhomogeneity compensation in structural brain imaging. Magn. Reson. Med. 2002; 47: 398–402.

101. Ulloa JL, Irarrazaval P, Hajnal JV. Exploring 3D RF shimming for slice selective imaging. Proceedings of the 13th Annual Meeting ISMRM, Miami Beach, FL, USA, 2005; 21.

102. Saekho S, Boada FE, Noll DC, Stenger VA. Small tip angle three-dimensional tailored radiofrequency slab-select pulse for reduced B_1 inhomogeneity at 3 T. Magn. Reson. Med. 2005; 53: 479–484.

103. Setsompop K, Wald LL, Alagappan V, Gagoski B, Hebrank F, Fontius U, Schmitt F, Adalsteinsson E. Parallel RF transmission with eight channels at 3 Tesla. Magn. Reson. Med. 2006; 56: 1163–1171.

104. Sbrizzi A, Hoogduin H, Lagendijk JJ, Luijten P, Sleijpen GLG, Van den Berg CAT. Time efficient design of multi dimensional RF pulses: application of a multi shift CGLS algorithm. Magn. Reson. Med. 2011; 66: 879–885.

105. Cloos MA, Boulant N, Luong M, Ferrand G, Giacomini E, Le Bihan D, Amadon A. kT-points: short three-dimensional tailored RF pulses for flip-angle homogenization over an extended volume. Magn. Reson. Med. 2012; 67: 72–80.

106. Malik SJ, Keihaninejad S, Hammers A, Hajnal JV. Tailored excitation in 3D with spiral nonselective (SPINS) RF pulses. Magn. Reson. Med. 2012; 67: 1303–1315.

107. Wu X, Schmitter S, Auerbach EJ, Uğurbil K, Van de Moortele PF. Mitigating transmit B_1 inhomogeneity in the liver at 7 T using multispoke parallel transmit RF pulse design. Quant. Imaging Med. Surg. 2014; 4: 4–10.

108. Cloos MA, Boulant N, Luong M, Ferrand G, Giacomini E, Hang MF, Wiggins CJ, Le Bihan D, Amadon A. Parallel-transmission-enabled magnetization-prepared rapid gradient-echo T1-weighted imaging of the human brain at 7 T. Neuroimage 2012; 62: 2140–2150.

109. Hoogduin H, Mooiweer R, Mens G, Hajnal JV, Luijten PR, Malik SJ. Initial experience with SPIral Non Selective (SPINS) RF pulses for homogeneous excitation at 7 T. Proceedings of the Joint Annual Meeting ISMRM-ESMRMB, Milan, Italy, 2014; 4914.

110. Ullmann P, Junge S, Wick M, Ruhm W, Hennig J. Experimental verification of transmit SENSE with simultaneous RF-transmission on multiple channels. Proceedings of the 13th Annual Meeting ISMRM, Miami Beach, FL, USA, 2005; 15.

111. Ullmann P, Schubert F, Haueisen R, Junge S, Seifert F, Wick M, Ruhm W, Hennig J. Flexible feature specific inner-volume selection with transmit SENSE: methods and applications in humans, animals and biological samples. Proceedings of the 14th Annual Meeting ISMRM, Seattle, WA, USA, 2006; 598.

112. Schneider JT, Haas M, Hennig J, Junge S, Ruhm W, Ullmann P. In-vivo flow-artifact suppression using parallel spatially selective excitation. Proceedings of the 17th Annual Meeting ISMRM, Honolulu, HI, USA, 2009; 4606.

113. Mooiweer R, Sbrizzi A, el Aidi H, Van den Berg CAT, Visser F, Leiner T, Luijten PR, Hoogduin H. Spatially selective excitation applied to aortic vessel wall imaging. Proceedings of the 21st Annual Meeting ISMRM, Salt Lake City, UT, USA, 2013; 4244.

114. Mooiweer R, Sbrizzi A, Visser F, Van den Berg CAT, Luijten PR, Hoogduin H. High resolution imaging of the hippocampus with spatially selective excitation and a reduced FOV readout at 7 T.

Proceedings of the 21st Annual Meeting ISMRM, Salt Lake City, UT, USA, 2013; 3016.

115. Mitsouras D, Mulkern RV, Rybicki FJ. Strategies for inner volume 3D fast spin echo magnetic resonance imaging using nonselective refocusing radio frequency pulses. Med. Phys. 2006; 33: 173–186.

116. Malik SJ, Hajnal JV. 3D-FSE inner volume imaging using 3D selective excitation. Proceedings of the Joint Annual Meeting ISMRM-ESMRMB, Milan, Italy, 2014; 948.

117. Thierfelder KM, Sommer WH, Dietrich O, Meinel FG, Theisen D, Paprottka PM, Strobl FF, Pfeuffer J, Reiser MF, Nikolaou K. Parallel-transmit-accelerated spatially-selective excitation MRI for reduced-FOV diffusion-weighted-imaging of the pancreas. Eur. J. Radiol. 2014; 83: 1709–1714.

118. Thierfelder KM, Scherr MK, Notohamiprodjo M, Weiß J, Dietrich O, Mueller-Lisse UG, Pfeuffer J, Nikolaou K, Theisen D. Diffusion-weighted MRI of the prostate: advantages of zoomed EPI with parallel-transmit-accelerated 2D-selective excitation imaging. Eur. Radiol. 2014; 24: 3233–3241.

119. Seeger A, Klose U, Bischof F, Strobel J, Ernemann U, Hauser T-K. Zoomed EPI DWI of acute spinal ischemia using a parallel transmission system. Clin. Neuroradiol. 2014.

120. Meyer CH, Pauly JM, Macovski A, Nishimura DG. Simultaneous spatial and spectral selective excitation. Magn. Reson. Med. 1990; 15: 287–304.

121. Malik SJ, Larkman DJ, O'Regan DP, Hajnal JV. Subject-specific water-selective imaging using parallel transmission. Magn. Reson. Med. 2010; 63: 988–997.

122. Setsompop K, Alagappan V, Gagoski BA, Potthast A, Hebrank F, Fontius U, Schmitt F, Wald LL, Adalsteinsson E. Broadband slab selection with B_1^+ mitigation at 7 T via parallel spectral-spatial excitation. Magn. Reson. Med. 2009; 61: 493–500.

123. Brunner D, Pruessmann K. Increasing bandwidth of spatially selective transmit SENSE pulses using constrained optimization. Proceedings of the 16th Annual Meeting ISMRM, Toronto, ON, Canada, 2008; 615.

124. Kerr AB, Etezadi-Amoli M, Fautz HP, Vogel MW, Gross P, Zhu Y, Pauly JM. Dual-band RF shimming at high-field with parallel excitation. Proceedings of the 16th Annual Meeting ISMRM, Toronto, QC, Canada, 2008; 617.

125. Deng W, Yang C, Alagappan V, Wald LL, Boada FE, Stenger VA. Simultaneous z-shim method for reducing susceptibility artifacts with multiple transmitters. Magn. Reson. Med. 2009; 61: 255–259.

126. Yang C, Deng W, Alagappan V, Wald LL, Stenger VA. Four-dimensional spectral-spatial RF pulses for simultaneous correction of B_1^+ inhomogeneity and susceptibility artifacts in T2*-weighted MRI. Magn. Reson. Med. 2010; 64: 1–8.

127. Zheng H, Zhao T, Qian Y, Schirda C, Ibrahim TS, Boada FE. Multi-slice parallel transmission three-dimensional tailored RF (PTX 3DTRF) pulse design for signal recovery in ultra high field functional MRI. J. Magn. Reson. 2013; 228: 37–44.

128. Larkman DJ, Hajnal JV, Herlihy AH, Coutts GA, Young IR, Ehnholm G. Use of multicoil arrays for separation of signal from multiple slices simultaneously excited. J. Magn. Reson. Imaging 2001; 13: 313–317.

129. Uğurbil K, Xu J, Auerbach EJ, Moeller S, Vu AT, Duarte-Carvajalino JM, Lenglet C, Wu X, Schmitter S, Van de Moortele PF, Strupp J, Sapiro G, De Martino F, Wang D, Harel N, Garwood M, Chen L, Feinberg DA, Smith SM, Miller KL, Sotiropoulos SN, Jbabdi S, Andersson JLR, Behrens TEJ, Glasser MF, Van Essen DC, Yacoub E. Pushing spatial and temporal resolution for functional and diffusion MRI in the Human Connectome Project. Neuroimage 2013; 80: 80–104.

130. Katscher U, Eggers H, Graesslin I, Mens G, Börnert P. 3D RF shimming using multi-frequency excitation. Proceedings of the 16th Annual Meeting ISMRM, Toronto, QC, Canada, 2008; 1311.

131. Wu X, Schmitter S, Auerbach EJ, Moeller S, Uğurbil K, Van de Moortele PF. Simultaneous multislice multiband parallel radiofrequency excitation with independent slice-specific transmit B_1 homogenization. Magn. Reson. Med. 2013; 70: 630–638.

132. Sharma A, Bammer R, Stenger VA, Grissom WA. Low peak power multiband spokes pulses for B_1^+ inhomogeneity-compensated simultaneous multislice excitation in high field MRI. Magn. Reson. Med. 2014.

133. Guérin B, Setsompop K, Ye H, Poser BA, Stenger AV, Wald LL. Design of parallel transmission pulses for simultaneous multislice with

explicit control for peak power and local specific absorption rate. Magn. Reson. Med. 2015; 73: 1946–1953.

134. Poser BA, Anderson RJ, Guérin B, Setsompop K, Deng W, Mareyam A, Serano P, Wald LL, Stenger VA. Simultaneous multislice excitation by parallel transmission. Magn. Reson. Med. 2014; 71: 1416–1427.

135. Schmitter S, Wu X, Uğurbil K, Van de Moortele PF. Design of parallel transmission radiofrequency pulses robust against respiration in cardiac MRI at 7 Tesla. Magn. Reson. Med. 2014.

136. Saekho S, Yip C, Noll DC, Boada FE, Stenger VA. Fast-kz three-dimensional tailored radiofrequency pulse for reduced B₁ inhomogeneity. Magn. Reson. Med. 2006; 55: 719–724.

137. Yip C, Grissom WA, Fessler JA, Noll DC. Joint design of trajectory and RF pulses for parallel excitation. Magn. Reson. Med. 2007; 58: 598–604.

138. Liu Y, Ji JX. Minimal-SAR RF pulse optimization for parallel transmission in MRI. *Proceedings of the 30th Annual Conference IEEE Engineering in Medicine and Biology Society*, Vancouver, BC, Canada, 2008; 5774–5777.

139. Davids M, Guérin B, Schad LR, Wald LL. Optimization of fast k-space trajectories for 3D spatially selective parallel excitations. *Proceedings of the Joint Annual Meeting ISMRM-ESMRMB*, Milan, Italy, 2014; 1452.

140. Zelinski AC, Wald LL, Setsompop K, Goyal VK, Adalsteinsson E. Sparsity-enforced slice-selective MRI RF excitation pulse design. IEEE Trans. Med. Imaging 2008; 27: 1213–1229.

141. Ma C, Xu D, King KF, Liang ZP. Joint design of spoke trajectories and RF pulses for parallel excitation. Magn. Reson. Med. 2011; 65: 973–985.

142. Yoon D, Fessler JA, Gilbert AC, Noll DC. Fast joint design method for parallel excitation radiofrequency pulse and gradient waveforms considering off-resonance. Magn. Reson. Med. 2012; 68: 278–285.

143. Xu D, King KF, Liang ZP. Variable slew-rate spiral design: theory and application to peak B₁ amplitude reduction in 2D RF pulse design. Magn. Reson. Med. 2007; 58: 835–842.

144. Hargreaves BA, Cunningham CH, Nishimura DG, Conolly SM. Variable-rate selective excitation for rapid MRI sequences. Magn. Reson. Med. 2004; 52: 590–597.

145. Shao T, Xia L, Tao G, Chi J, Liu F, Crozier S. Advanced three-dimensional tailored RF pulse design in volume selective parallel excitation. IEEE Trans. Med. Imaging 2012; 31: 997–1007.

146. Schneider R, Haueisen J, Pfeuffer J. Shaped saturation with inherent radiofrequency-power-efficient trajectory design in parallel transmission. Magn. Reson. Med. 2014; 72: 1015–1027.

147. Lee D, Lustig M, Grissom WA, Pauly JM. Time-optimal design for multidimensional and parallel transmit variable-rate selective excitation. Magn. Reson. Med. 2009; 61: 1471–1479.

148. Lustig M, Kim SJ, Pauly JM. A fast method for designing time-optimal gradient waveforms for arbitrary-space trajectories. IEEE Trans. Med. Imaging 2008; 27: 866–873.

149. Lee D, Grissom WA, Lustig M, Kerr AB, Stang PP, Pauly JM. VERSE-guided numerical RF pulse design: a fast method for peak RF power control. Magn. Reson. Med. 2012; 67: 353–362.

150. Schneider J, Haas M, Hennig J, Junge S, Ruhm W, Ullmann P. Coping with off-resonance effects and gradient imperfections in parallel transmission experiments. *Proceedings of the 17th Annual Meeting ISMRM*, Honolulu, HI, USA, 2009; 172.

151. Wu X, Vaughan JT, Uğurbil K, Van de Moortele PF. Parallel excitation in the human brain at 9.4 T counteracting k-space errors with RF pulse design. Magn. Reson. Med. 2010; 63: 524–529.

152. Schneider JT, Haas M, Ruhm W, Hennig J, Ullmann P. Robust spatially selective excitation using radiofrequency pulses adapted to the effective spatially encoding magnetic fields. Magn. Reson. Med. 2011; 65: 409–421.

153. Addy NO, Wu HH, Nishimura DG. Simple method for MR gradient system characterization and k-space trajectory estimation. Magn. Reson. Med. 2012; 68: 120–129.

154. Vannesjo SJ, Haeberlin M, Kasper L, Pavan M, Wilm BJ, Barmet C, Pruessmann KP. Gradient system characterization by impulse response measurements with a dynamic field camera. Magn. Reson. Med. 2013; 69: 583–593.

155. Harkins KD, Does MD, Grissom WA. Iterative method for predistortion of MRI gradient waveforms. IEEE Trans. Med. Imaging 2014; 33: 1641–1647.

156. Papadakis NG, Wilkinson AA, Carpenter TA, Hall LD. A general method for measurement of the time integral of variant magnetic field gradients: application to 2D spiral imaging. Magn. Reson. Imaging 1997; 15: 567–578.

157. De Zanche N, Barmet C, Nordmeyer-Massner JA, Pruessmann KP. NMR probes for measuring magnetic fields and field dynamics in MR systems. Magn. Reson. Med. 2008; 60: 176–186.

158. Pauly J, Nishimura D, Macovski A. A linear class of large-tip-angle selective excitation pulses. J. Magn. Reson. 1989; 82: 571–587.

159. Pauly J, Le Roux P, Nishimura D, Macovski A. Parameter relations for the Shinnar-Le Roux selective excitation pulse design algorithm. IEEE Trans. Med. Imaging 1991; 10: 53–65.

160. Shinnar M, Eleff S, Subramanian H, Leigh JS. The synthesis of pulse sequences yielding arbitrary magnetization vectors. Magn. Reson. Med. 1989; 12: 74–80.

161. Grissom WA, McKinnon GC, Vogel MW. Nonuniform and multidimensional Shinnar-Le Roux RF pulse design method. Magn. Reson. Med. 2012; 68: 690–702.

162. Grissom WA, Yip C, Wright SM, Fessler JA, Noll DC. Additive angle method for fast large-tip-angle RF pulse design in parallel excitation. Magn. Reson. Med. 2008; 59: 779–787.

163. Zheng H, Zhao T, Qian Y, Ibrahim TS, Boada FE. Improved large tip angle parallel transmission pulse design through a perturbation analysis of the bloch equation. Magn. Reson. Med. 2011; 66: 687–696.

164. Collins CM, Wang Z, Mao W, Fang J, Liu W, Smith MB. Array-optimized composite pulse for excellent whole-brain homogeneity in high-field MRI. Magn. Reson. Med. 2007; 57: 470–474.

165. Conolly S, Nishimura D, Macovski A. Optimal control solutions to the magnetic resonance selective excitation problem. IEEE Trans. Med. Imaging 1986; 5: 106–115.

166. Xu D, King KF, Zhu Y, McKinnon GC, Liang ZP. Designing multichannel, multidimensional, arbitrary flip angle RF pulses using an optimal control approach. Magn. Reson. Med. 2008; 59: 547–560.

167. Grissom WA, Xu D, Kerr AB, Fessler JA, Noll DC. Fast large-tip-angle multidimensional and parallel RF pulse design in MRI. IEEE Trans. Med. Imaging 2009; 28: 1548–1559.

168. Vinding MS, Maximov II, Tošner Z, Nielsen NC. Fast numerical design of spatial-selective rf pulses in MRI using Krotov and quasi-Newton based optimal control methods. J. Chem. Phys. 2012; 137: 054203.

169. Hennig J, Welz AM, Schultz G, Korvink J, Liu Z, Speck O, Zaitsev M. Parallel imaging in non-bijective, curvilinear magnetic field gradients: a concept study. Magn. Reson. Mater. Phys. Biol. Med. 2008; 21: 5–14.

170. Stockmann JP, Ciris PA, Galiana G, Tam L, Constable RT. O-space imaging: highly efficient parallel imaging using second-order nonlinear fields as encoding gradients with no phase encoding. Magn. Reson. Med. 2010; 64: 447–456.

171. Haas M, Ullmann P, Schneider JT, Post H, Ruhm W, Hennig J, Zaitsev M. PexLoc—Parallel excitation using local encoding magnetic fields with nonlinear and nonbijective spatial profiles. Magn. Reson. Med. 2013; 70: 1220–1228.

172. Homann H, Graesslin I, Nehrke K, Findeklee C, Dössel O, Börnert P. Specific absorption rate reduction in parallel transmission by k-space adaptive radiofrequency pulse design. Magn. Reson. Med. 2011; 65: 350–357.

173. Orzada S, Maderwald S, Poser BA, Bitz AK, Quick HH, Ladd ME. RF excitation using time interleaved acquisition of modes (TIAMO) to address B₁ inhomogeneity in high-field MRI. Magn. Reson. Med. 2010; 64: 327–333.

174. Orzada S, Maderwald S, Poser BA, Johst S, Kannengiesser S, Ladd ME, Bitz AK. Time-interleaved acquisition of modes: an analysis of SAR and image contrast implications. Magn. Reson. Med. 2012; 67: 1033–1041.

175. Xu D, King KF. Joint design of excitation and refocusing pulses for fast spin echo sequences in parallel transmission. *Proceedings of the 17th Annual Meeting ISMRM*, Honolulu, HI, USA, 2009; 174.

176. Sun H, Fessler JA, Noll DC, Nielsen JF. Strategies for improved 3D small-tip fast recovery imaging. Magn. Reson. Med. 2014; 72: 389–398.

177. Malik SJ, Padormo F, Price AN, Hajnal JV. Spatially resolved extended phase graphs: modeling and design of multipulse sequences with parallel transmission. Magn. Reson. Med. 2012; 68: 1481–1494.

178. Hennig J. Multiecho imaging sequences with low refocusing flip angles. J. Magn. Reson. 1988; 407: 397–407.

179. Malik SJ, Beqiri A, Padormo F, Hajnal JV. Direct signal control of the steady-state response of 3D-FSE sequences. Magn. Reson. Med. 2015; 73: 951–963.

180. Eggenschwiler F, O'Brien KR, Gruetter R, Marques JP. Improving T2-weighted imaging at high field through the use of kT-points. Magn. Reson. Med. 2014; 71: 1478–1488.

181. Massire A, Vignaud A, Robert B, Le Bihan D, Boulant N, Amadon A. Parallel-transmission-enabled three-dimensional T2-weighted imaging of the human brain at 7 Tesla. Magn. Reson. Med. 2014.

182. Eggenschwiler F, O'Brien KR, Maréchal B, Gruetter R, Marques JP. Dynamic kT-points: a new concept to improve T2-weighted imaging at 7 T. Proceedings of the Joint Annual Meeting ISMRM-ESMRMB, Milan, Italy, 2014; 4330.

183. Zhu Y, Alon L, Deniz CM, Brown R, Sodickson DK. System and SAR characterization in parallel RF transmission. Magn. Reson. Med. 2012; 67: 1367–1378.

184. Katscher U, Findeklee C, Voigt T. B1-based specific energy absorption rate determination for nonquadrature radiofrequency excitation. Magn. Reson. Med. 2012; 68: 1911–1918.

185. Zhang X, Schmitter S, Van de Moortele PF, Liu J, He B. From complex B1 mapping to local SAR estimation for human brain MR imaging using multi-channel transceiver coil at 7 T. IEEE Trans. Med. Imaging 2013; 32: 1058–1067.

186. Buchenau S, Haas M, Splitthoff DN, Hennig J, Zaitsev M. Iterative separation of transmit and receive phase contributions and B1+-based estimation of the specific absorption rate for transmit arrays. Magn. Reson. Mater. Phys. Biol. Med. 2013; 26: 463–476.

187. Alon L, Deniz CM, Brown R, Sodickson DK, Zhu Y. Method for in situ characterization of radiofrequency heating in parallel transmit MRI. Magn. Reson. Med. 2013; 69: 1457–1465.

188. Bardati F, Borrani A, Gerardino A, Lovisolo GA. SAR optimization in a phased array radiofrequency hyperthermia system. IEEE Trans. Biomed. Eng. 1995; 42: 1201–1207.

189. Dimbylow PJ. FDTD calculations of the whole-body averaged SAR in an anatomically realistic voxel model of the human body from 1 MHz to 1 GHz. Phys. Med. Biol. 1997; 42: 479.

190. Eichfelder G, Gebhardt M. Local specific absorption rate control for parallel transmission by virtual observation points. Magn. Reson. Med. 2011; 66: 1468–1476.

191. Sbrizzi A, Hoogduin H, Lagendijk JJ, Luijten P, Sleijpen GLG, Van den Berg CAT. Fast design of local N-gram-specific absorption rate-optimized radiofrequency pulses for parallel transmit systems. Magn. Reson. Med. 2012; 67: 824–834.

192. Wolf S, Diehl D, Gebhardt M, Mallow J, Speck O. SAR simulations for high-field MRI: how much detail, effort, and accuracy is needed? Magn. Reson. Med. 2013; 69: 1157–1168.

193. Homann H, Börnert P, Eggers H, Nehrke K, Dössel O, Graesslin I. Toward individualized SAR models and in vivo validation. Magn. Reson. Med. 2011; 66: 1767–1776.

194. Jin J, Liu F, Weber E, Crozier S. Improving SAR estimations in MRI using subject-specific models. Phys. Med. Biol. 2012; 57: 8153–8171.

195. De Greef M, Ipek O, Raaijmakers AJE, Crezee J, Van den Berg CAT. Specific absorption rate intersubject variability in 7 T parallel transmit MRI of the head. Magn. Reson. Med. 2013; 69: 1476–1485.

196. Voigt T, Homann H, Katscher U, Doessel O. Patient-individual local SAR determination: in vivo measurements and numerical validation. Magn. Reson. Med. 2012; 68: 1117–1126.

197. Oh S, Ryu Y, Carluccio G, Sica CT, Collins CM. Measurement of SAR-induced temperature increase in a phantom and in vivo with comparison to numerical simulation. Magn. Reson. Med. 2014; 71: 1923–1931.

198. Zelinski AC, Angelone LM, Goyal VK, Bonmassar G, Adalsteinsson E, Wald LL. Specific absorption rate studies of the parallel transmission of inner-volume excitations at 7 T. J. Magn. Reson. Imaging, 2008; 28: 1005–1018.

199. Beqiri A, Padormo F, Hand JW, Hajnal JV, Malik SJ. SAR optimised local B1+ shimming for cardiac imaging at 3 T – a multi-model study. Proceedings of the Joint Annual Meeting ISMRM-ESMRMB, Milan, Italy, 2014; 179.

200. Etezadi-Amoli M, Stang P, Kerr A, Pauly J, Scott G. Controlling radiofrequency-induced currents in guidewires using parallel transmit. Magn. Reson. Med. 2014.

201. Eryaman Y, Guerin B, Akgun C, Herraiz JL, Martin A, Torrado-Carvajal A, Malpica N, Hernandez-Tamames JA, Schiavi E, Adalsteinsson E, Wald LL. Parallel transmit pulse design for patients with deep brain stimulation implants. Magn. Reson. Med. 2015; 73: 1896–1903.

202. Eryaman Y, Akin B, Atalar E. Reduction of implant RF heating through modification of transmit coil electric field. Magn. Reson. Med. 2011; 65: 1305–1313.

203. Graesslin I, Krueger S, Vernickel P, Achtzehn J, Nehrke K, Weiss S. Detection of RF unsafe devices using a parallel transmission MR system. Magn. Reson. Med. 2013; 70: 1440–1449.

204. Alagappan V, Nistler J, Adalsteinsson E, Setsompop K, Fontius U, Zelinski A, Vester M, Wiggins GC, Hebrank F, Renz W, Schmitt F, Wald LL. Degenerate mode band-pass birdcage coil for accelerated parallel excitation. Magn. Reson. Med. 2007; 57: 1148–1158.

205. Setsompop K, Wald LL. SAR reduction through dark modes excitation. Proceedings of the 19th Annual Meeting ISMRM, Montreal, QC, Canada, 2011; 3890.

206. Eryaman Y, Guerin B, Keil B, Mareyam A, Herraiz JL, Kosior RK, Martin A, Torrado-Carvajal A, Malpica N, Hernandez-Tamames JA, Schiavi E, Adalsteinsson E, Wald LL. SAR reduction in 7 T C-spine imaging using a "dark modes" transmit array strategy. Magn. Reson. Med. 2015; 73: 1533–1539.

207. Lattanzi R, Sodickson DK. Ideal current patterns yielding optimal signal-to-noise ratio and specific absorption rate in magnetic resonance imaging: computational methods and physical insights. Magn. Reson. Med. 2012; 68: 286–304.

208. Insko EK, Bolinger L. Mapping of the radiofrequency field. J. Magn. Reson. A 1993; 103: 82–85.

209. Yarnykh VL. Actual flip-angle imaging in the pulsed steady state: a method for rapid three-dimensional mapping of the transmitted radiofrequency field. Magn. Reson. Med. 2007; 57: 192–200.

210. Sacolick LI, Wiesinger F, Hancu I, Vogel MW. B1 mapping by Bloch–Siegert shift. Magn. Reson. Med. 2010; 63: 1315–1322.

211. Nehrke K, Börnert P. DREAM—a novel approach for robust, ultrafast, multislice B1 mapping. Magn. Reson. Med. 2012; 68: 1517–1526.

212. Fautz HP, Vogel M, Gross P, Kerr A, Zhu Y. B1 mapping of coil arrays for parallel transmission. Proceedings of the 16th Annual Meeting ISMRM, Toronto, ON, Canada, 2008; 1247.

213. Nehrke K, Versluis MJ, Webb A, Börnert P. Volumetric B1+ mapping of the brain at 7 T using DREAM. Magn. Reson. Med. 2014; 71: 246–256.

214. Van de Moortele PF, Snyder C, DelaBarre L, Adriany G, Vaughan J, Ugurbil K. Calibration tools for RF shim at very high field with multiple element RF coils: from ultra fast local relative phase to absolute magnitude B1+ mapping. Proceedings of the Joint Annual Meeting ISMRM-ESMRMB, Berlin, Germany, 2007; 1676.

215. Setsompop K, Alagappan V, Gagoski B, Witzel T, Polimeni J, Potthast A, Hebrank F, Fontius U, Schmitt F, Wald LL, Adalsteinsson E. Slice-selective RF pulses for in vivo B1+ inhomogeneity mitigation at 7 tesla using parallel RF excitation with a 16-element coil. Magn. Reson. Med. 2008; 60: 1422–1432.

216. Morrell GR, Schabel MC. An analysis of the accuracy of magnetic resonance flip angle measurement methods. Phys. Med. Biol. 2010; 55: 6157–6174.

217. Nehrke K, Börnert P. Improved B1-mapping for multi RF transmit systems. Proceedings of the 16th Annual Meeting ISMRM, Toronto, ON, Canada, 2008; 353.

218. Brunner DO, Pruessmann KP. B1+ interferometry for the calibration of RF transmitter arrays. Magn. Reson. Med. 2009; 61: 1480–1488.

219. Malik SJ, Larkman DJ, Hajnal JV. Optimal linear combinations of array elements for B1 mapping. Magn. Reson. Med. 2009; 62: 902–909.

220. Tse DHY, Poole MS, Magill AW, Felder J, Brenner D, Shah NJ. Encoding methods for mapping in parallel transmit systems at ultra high field. J. Magn. Reson. 2014; 245: 125–132.

221. Schneider JT, Kalayciyan R, Haas M, Herrmann SR, Ruhm W, Hennig J, Ullmann P. Inner-volume imaging in vivo using three-dimensional parallel spatially selective excitation. Magn. Reson. Med. 2013; 69: 1367–1378.

© 2015 The Authors. NMR in Biomedicine published by John Wiley & Sons Ltd. wileyonlinelibrary.com/journal/nbm